10/9/95

SANDIA REPORT

SAND92–0252 • UC–900
Unlimited Release
Printed May 1995

Final Report:

Aerosol Formation from High-Velocity Uranium Drops: Comparison of Number and Mass Distributions

D. J. Rader, D. A. Benson

Prepared by
Sandia National Laboratories
Albuquerque, New Mexico 87185 and Livermore, California 94550
for the United States Department of Energy
under Contract DE-AC04-94AL85000

SF2900Q(8-81)

Issued by Sandia National Laboratories, operated for the United States Department of Energy by Sandia Corporation.

Available to DOE and DOE contractors from
Office of Scientific and Technical Information
PO Box 62
Oak Ridge, TN 37831

Prices available from (615) 576-8401, FTS 626-8401

Available to the public from
National Technical Information Service
US Department of Commerce
5285 Port Royal Rd
Springfield, VA 22161

NTIS price codes
Printed copy: A04
Microfiche copy: A01

DISCLAIMER

Portions of this document may be illegible in electronic image products. Images are produced from the best available original document.

REPORT DOCUMENTATION PAGE

Form Approved
OMB No. 0704-0188

1. AGENCY USE ONLY (Leave blank)	2. REPORT DATE	3. REPORT TYPE AND DATES COVERED
		Final - 10/91-3/93

4. TITLE AND SUBTITLE
Final Report: Aerosol Formation from High-Velocity Uranium Drops: Comparison of Number and Mass Distributions

5. FUNDING NUMBERS
HHM440-9-9035

6. AUTHOR(S)
D. J. Rader and D. A. Benson

7. PERFORMING ORGANIZATION NAME(S) AND ADDRESS(ES)
Sandia National Laboratories
Department 1512, MS0834
P. O. Box 5800
Albuquerque, NM 87185-0834

8. PERFORMING ORGANIZATION REPORT NUMBER
SAND92-0252

9. SPONSORING/MONITORING AGENCY NAME(S) AND ADDRESS(ES)
Department of Defense
The Pentagon
Washington, DC 20340-6160

10. SPONSORING/MONITORING AGENCY REPORT NUMBER
N/A

11. SUPPLEMENTARY NOTES
N/A

12a. DISTRIBUTION/AVAILABILITY STATEMENT
Unlimited

12b. DISTRIBUTION CODE
N/A

13. ABSTRACT *(Maximum 200 words)*

This report presents the results of an experimental study of the aerosol produced by the combustion of high-velocity, molten-uranium droplets produced by the simultaneous heating and electromagnetic launch of uranium wires. These tests are intended to simulate the reduction of high-velocity fragments into aerosol in high-explosive detonations or reactor accidents involving nuclear materials. As reported earlier, the resulting aerosol consists mainly of web-like chain agglomerates. A condensation nucleus counter was used to investigate the decay of the total particle concentration due to coagulation and losses. Number size distributions based on mobility equivalent diameter obtained soon after launch with a Differential Mobility Particle Sizer showed lognormal distributions with an initial count median diameter (CMD) of 0.3 μm and a geometric standard deviation, σg of about 2; the CMD was found to increase and σg decrease and time due to coagulation. Mass size distributions with mass median aerodynamic diameters of about 0.5 μm and an aerodynamic geometric standard deviation of about 2. Approximate methods for converting between number and mass distributions and between mobility and aerodynamic equivalent diameters are presented.

14. SUBJECT TERMS	15. NUMBER OF PAGES
Aerosol, Combustion, Chain Agglomerates, Fractal Coagulation	57
	16. PRICE CODE

17. SECURITY CLASSIFICATION OF REPORT	18. SECURITY CLASSIFICATION OF THIS PAGE	19. SECURITY CLASSIFICATION OF ABSTRACT	20. LIMITATION OF ABSTRACT
Unclassified	Unclassified	Unclassified	Same as Report

NSN 7540-01-280-5500

Standard Form 298 (Rev. 2-89)
Prescribed by ANSI Std. Z39-18
298-102

BLANK PAGE

SAND92-0252
Unlimited Release
Printed May 1995

Distribution
Category UC-900

Final Report:

Aerosol Formation from High-Velocity Uranium Drops: Comparison of Number and Mass Distributions*

D. J. Rader
Energetic and Multiphase Processes

D. A. Benson
Advanced Packaging Department

Sandia National Laboratories
Albuquerque, New Mexico 87185-0834

Abstract

This report presents the results of an experimental study of the aerosol produced by the combustion of high-velocity molten-uranium droplets produced by the simultaneous heating and electromagnetic launch of uranium wires. These tests are intended to simulate the reduction of high-velocity fragments into aerosol in high-explosive detonations or reactor accidents involving nuclear materials. As reported earlier, the resulting aerosol consists mainly of web-like chain agglomerates. A condensation nucleus counter was used to investigate the decay of the total particle concentration due to coagulation and losses. Number size distributions based on mobility equivalent diameter obtained soon after launch with a Differential Mobility Particle Sizer showed lognormal distributions with an initial count median diameter (CMD) of 0.3 μm and a geometric standard deviation, σ_g of about 2; the CMD was found to increase and σ_g decrease with time due to coagulation. Mass size distributions based on aerodynamic diameter were obtained for the first time with a Microorifice Uniform Deposit Impactor, which showed lognormal distributions with mass median aerodynamic diameters of about 0.5 μm and an aerodynamic geometric standard deviation of about 2. Approximate methods for converting between number and mass distributions and between mobility and aerodynamic equivalent diameters are presented.

This work performed for the U.S. Department of Defense
by Sandia National Laboratories, Albuquerque, NM 87185

BLANK PAGE

CONTENTS

List of Figures

List of Tables

EXECUTIVE SUMMARY

This report documents an experimental study of the aerosol production from the high-velocity combustion of uranium-1.5 wt% molybdenum alloy droplets. An electromagnetic launcher was used to simultaneously heat to melting and electromagnetically propel uranium alloy wires at velocities of about 100 m/s. After launch, the combustion products that are left behind in the droplet wakes cool and condense on existing particles or nucleate to form very high concentrations of ultrafine particles. These primary particles rapidly coagulate to form web-like agglomerates. Simultaneously, mixing acts to spread the particles around the chamber. Even after the aerosol is mixed throughout the entire chamber volume, concentrations are high enough that coagulation continues to occur. The size distribution also changes due to loss mechanisms, including particle removal by the sampling equipment and particle losses to the chamber walls by sedimentation and diffusion. This work applied a variety of aerosol diagnostics to provide as much information as possible regarding the aerosol dynamics taking place within the chamber.

Direct concentration measurements with a Condensation Nucleus Counter (CNC) provided several valuable insights into the dynamics of this combustion-generated aerosol. Most important is that the concentration is not constant, but decays with time as a result of coagulation, sampling losses, and wall losses. The most rapid decay is seen immediately after launch, when the combination of small particle size and high concentration leads to rapid coagulation. An approximate model that includes coagulation, wall losses, and sampling losses is proposed to describe the dynamics of the concentration decay. Soon after launch, coagulation dominates, and a best-fit coagulation coefficient for this time is about 1×10^{-7} cm^3/min. Although there is a large uncertainty in this value, it is significantly greater than for spheres with the same Differential Mobility Particle Sizer (DMPS)-measured diameters. Thus, coagulation rates of similar aerosol in the field may be significantly higher than expected. The cause of this enhanced coagulation rate is likely the chain agglomerate structure of the particles which provides a larger surface area for a given mass. The model also does a good job of describing late-time losses, which are dominated by the sampling of aerosol from the chamber to make measurements. Thus, at late times both wall losses and coagulation can be neglected. One concern is the relatively large fluctuations observed during the CNC tests, which suggests that the sampling chamber was not well mixed.

DMPS tests supported results from previous launcher studies (Benson and Rader, 1986; Rader and Benson, 1988; Benson and Rader, 1990) and also provided new results. As shown for other metals, the agglomerates generated by the high-velocity combustion of uranium alloy droplets can be adequately described by a simple lognormal number distribution. The size distributions are very similar to those observed for earlier tests with tungsten: both give early-time CMDs of 0.3 - 0.4 μm with geometric standard deviations of about 2, although concentrations for the tungsten tests were at least two orders of magnitude less than in the present uranium tests. A major advance in the present work was the use of a new charging algorithm, which greatly improved the agreement between DMPS best-fit predictions and CNC direct measurements of the total concentration. In

addition, DMPS measurements have demonstrated that the size distribution grows in size and narrows in spread when coagulation is active.

The successful application of the Microorifice Uniform Deposit Impactor (MOUDI) in measuring this combustion generated aerosol has significantly added to our understanding in several ways. First, the MOUDI tests provided the first description of this aerosol in terms of a mass distribution based on aerodynamic diameter. The distribution of mass is essential in interpreting ensemble techniques (such as filter samples) which typically measure total mass. A description based on aerodynamic diameter is valuable as it is the appropriate characteristic diameter which governs inertial processes, such as sampling and transport efficiency, human respiration, and gravitational sedimentation. A mass distribution based on aerodynamic diameter is also needed in describing sedimentation losses within the sample chamber. Second, comparison of early and late time distributions confirms several observations based on DMPS measurements: lognormal size distributions that show increasing median diameter and decreasing geometric standard deviation with time due to coagulation. The rate of growth in terms of aerodynamic diameter, however, is much less than that in terms of mobility diameter. Finally, it also appears that the large-particle tails of both early- and late-time distributions are essentially identical, suggesting that removal by sedimentation may dominate other processes for the larger particles.

Direct comparisons between the DMPS and MOUDI require various assumptions regarding the fractal nature of the agglomerates and their size distribution. Under the lognormal assumption (which seems to hold acceptably well for the present aerosol), well-established formula relate the count and mass median diameters for the same equivalent diameter (e.g., for converting between aerodynamic count and mass median diameters). The comparison between mobility (DMPS-measured) and aerodynamic (impactor-measured) diameters requires additional analysis. Here, a new analysis is presented that is based on the assumption that the aerosol is fractal. The resulting analysis provided expressions that relate aerodynamic and mobility diameters and geometric standard deviations. Using this analysis, estimates are made of the proportionality constant relating particle mobility and mass (assuming a mass fractal dimension of two). One striking result is that the same particle will be sized about three times larger in the DMPS than in the MOUDI. The widths of the corrected-DMPS and MOUDI distributions are not in agreement; the cause of this discrepancy could either be experimental or model-related.

A major outcome of this work is that, due to the nonspherical nature of this aerosol, different "diameters" are required to describe each of the various mechanisms controlling the size distribution. Thus, the same agglomerate may settle under gravity at the same speed as a 1 μm sphere, while it diffuses at the same rate as a spherical particle several times larger. Although these issues were dealt with in the context of describing the aerosol evolution within the chamber, it should be emphasized that the same issues will arise in predicting the aerosol behavior in field environments. For example, dispersal characterization under accident scenarios and reconstruction of the explosive environment from particle samples collected from the debris cloud frequently require simultaneous modeling of coagulation, diffusion, and sedimentation. The present work provides methods for converting between the various equivalent diameters required for these calculations.

1.0 INTRODUCTION

This work continues an experimental study of the aerosol production from the high-velocity combustion of heavy metal droplets. The motivation for this work is the need to assess the radionuclide dispersal from a non-nuclear weapon detonation; applications include (1) reconstruction of the explosive environment from particles collected from a debris cloud and (2) dispersal characterization under accident scenarios. The focus of this work is the characterization of the submicron aerosol formed during droplet combustion, including its size distribution (both mass and number), morphology, and time evolution. Because of the highly nonspherical nature of these particles, extensive effort has been directed to describing the relationships between the aerosol mass and number distributions measured by different physical techniques. All of the results presented in this study are for a uranium-1.5 wt% molybdenum alloy.

Previous reports (Benson and Rader, 1986; Rader and Benson, 1988; Benson and Rader, 1990) describe the operation of an electromagnetic launcher device that is used to explore, in a lab environment, the break-up and combustion of molten metals. The present study uses a second-generation electromagnetic launcher (described in detail in Benson and Rader, 1990) to simultaneously melt and launch uranium alloy wires at velocities of about 100 m/s. The accelerated metal breaks up by aerodynamic forces to produce a distribution of molten droplets or solid particles moving at high velocity. The launcher permits independent control of droplet velocity and temperature over a wide range. The uranium-molybdenum sample is initially in the form of a wire (2.73 cm in length by 0.0564 cm diameter), mounted adjacent to a copper driver plate with a thin mylar insulator between them. A pulsed power system produces a current that flows through the driver plate and generates a magnetic field, while the current flowing in the opposite direction through the wire interacts with the magnetic field and simultaneously accelerates and melts the wire.

After launch, the uranium alloy droplets pass into and are confined by a test chamber consisting of four compartments each 64 cm long and 20 cm by 20 cm in cross section (details of the test chamber are described in Benson and Rader, 1990). A schematic of the launcher showing the four chambers is provided in Figure 1. The compartments are separated by fast closing shutters that are automatically closed by a pneumatic system after passage of the launched sample material. For uranium, a large fraction of the total mass transits the entire length of the test chamber and impacts a witness plate at the end of compartment four. A series of three apertures are placed near the launcher to collimate the molten material and prevent collisions with chamber walls. Each collimating aperture consists of a square cut-out in a copper plate. The plates are placed at distances of 5.1, 10.2, and 32.7 cm from the initial wire position in the launcher; the first and second apertures are 1.9 and 2.54 cm wide, respectively. The width of the final collimating aperture (farthest from the launcher) was varied in these tests to control the amount of molten material entering the sample chambers.

After the shutters close, the combustion products that are left behind in the droplet wakes cool and either condense on existing particles or nucleate to form very high concentrations of ultrafine particles. These primary particles rapidly coagulate to form the web-like agglomerates that have been previously reported (Benson and Rader, 1990), such as are

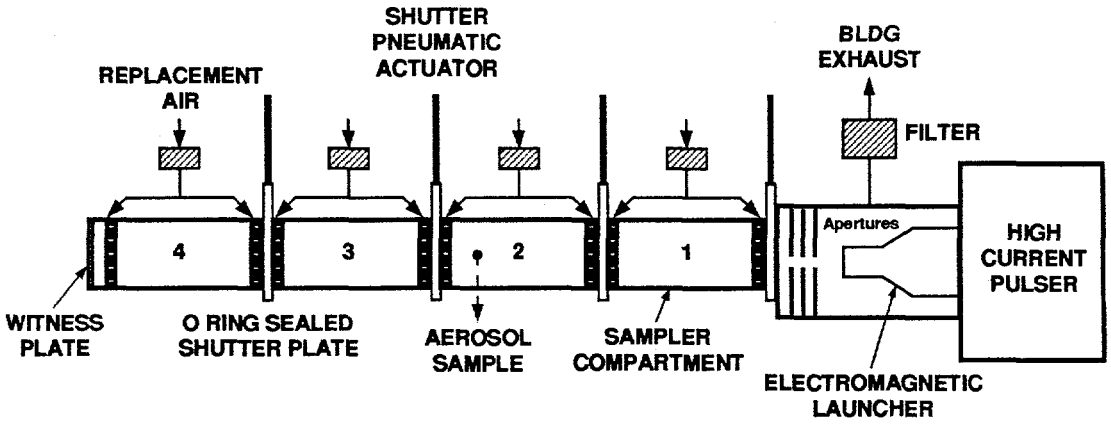

Figure 1. Schematic of the electromagnetic launcher and sample chamber.

shown in Figure 2. Simultaneously, mixing acts to spread the particles around the chamber (initially, all of the aerosol is contained in a very small volume corresponding to the wake regions behind the metal droplets). Even after the aerosol is mixed throughout the entire chamber volume, concentrations are high enough that coagulation continues to occur. The size distribution also changes due to loss mechanisms, including particle removal by the sampling equipment and particle losses to the chamber walls by sedimentation and diffusion. Interestingly, due to the nonspherical nature of this aerosol, different characteristic sizes[1] are required to describe each of the various physical mechanisms controlling the aerosol behavior. For example, a particular agglomerate may settle under gravity at the same speed as a 1 μm sphere, but diffuse at the same rate as a spherical particle several times larger. Although these issues are dealt with in the context of describing the aerosol evolution within the chamber, it should be emphasized that the same issues will arise in predicting the aerosol behavior in field environments. In this respect, this report describes the evolution of particle size distributions and how data from field tests may be interpreted in terms of the initial formation event.

After the launch and the shutters close, a variety of aerosol diagnostics are used to characterize the combustion aerosol. In all, 36 launches were made during which aerosol tests were conducted; a summary of all of the aerosol tests is given in Table 6 of Appendix A. Real-time measurements of size distribution and concentration were made

1. In this report, extensive use will be made of the concept of an *equivalent diameter*. Basically, a nonspherical particle is characterized by the equivalent diameter of a sphere that shares the same value of some physical property. For example, the *aerodynamic equivalent diameter*, d_{ae}, for a particle is defined as the diameter of a unit density sphere that falls at the same speed due to gravity as the given particle. Similarly, the *mobility equivalent diameter*, d_{me}, is defined as the diameter of a spherical particle that diffuses at the same rate as the given particle. Unfortunately, the mobility and aerodynamic equivalent diameters can differ significantly for a highly nonspherical particle (see Hinds, 1982).

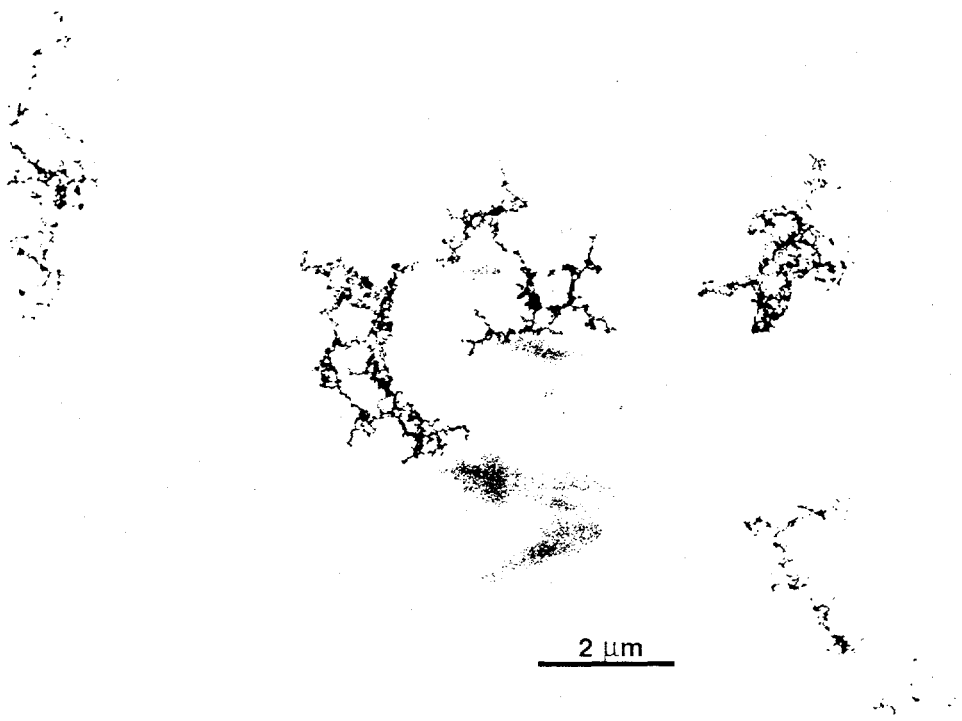

Figure 2. Scanning Electron Microscope images of fractal uranium particles that have been collected on a substrate using an electrostatic collector.

with the Differential Mobility Particle Sizer (DMPS), Condensation Nucleus Counter (CNC), and the Microorifice Uniform Deposit Impactor (MOUDI). In addition, filter samples were taken and weighed to determine the total mass loading in the chambers. Tests were also made in which size-selected samples (generated by the DMPS) were collected by an electrostatic precipitator directly onto TEM grids for later image analysis. These latter tests included launches into nitrogen and carbon dioxide environments. In general, this report summarizes data obtained by the real-time diagnostics: filter and TEM analysis are not reported here. Experimental results for the CNC, DMPS, and MOUDI are presented in Chapters 2, 3, and 4, respectively.

As in earlier studies of the evolution of tungsten and zirconium aerosols (Rader and Benson, 1988), the DMPS plays a key role in this study in characterizing the time evolution of the number distribution based on mobility equivalent diameter, d_{me}, for a uranium combustion aerosol. The mobility equivalent diameter based number distribution measured by the DMPS is of particular interest as it is needed to predict both particle diffusion and coagulation rates. In addition, the present work includes direct measurements of the total concentration using a CNC. The purpose of the CNC was to aid in obtaining the early-time coagulation rate and the late-time particle loss rate. This work also includes the first use of the MOUDI to characterize the mass distribution based on aerodynamic equivalent diameter for a uranium combustion aerosol. The aerodynamic diameter is important as it is the appropriate equivalent diameter to describe particle sedimentation, as well as inertial effects (such as large-particle deposition in a human lung or in a sampling system).

Due to the highly nonspherical nature of the combustion aerosol observed in these tests, the mobility and aerodynamic equivalent diameters characterizing the same aerosol will differ greatly. In addition, nonsphericity complicates the conversion between size distributions based on number (number of particles per cm^3 of air) and mass (mass of particles per cm^3 of air). Thus, an attempt is made to provide a theoretical framework for converting between number and mass median diameters, and between mobility and aerodynamic equivalent diameters (Chapter 4). The analysis relies heavily on the assumption of a fractal-like nature of the aerosol. Basically, a fractal description allows a relationship between particle size and volume that differs from the well-known result for a sphere: $V \propto d^3$. In particular, the fractal analysis for these web-like agglomerates results in an exponent value that is close to two (instead of three for a sphere). It should be stated that the present work has not rigorously proved the fractal nature of the present aerosol; a fractal structure is assumed and the implications are explored. As will be seen, the present data are at least qualitatively consistent with this assumption.

2.0 CONDENSATION NUCLEUS COUNTER

2.1 INTRODUCTION

This chapter describes tests designed to explore the time-dependent evolution of the combustion aerosol by using a Condensation Nucleus Counter (CNC) to measure the total concentration in the chamber. The intent of these tests was to find some simple correlation between total concentration and time. A test matrix was conducted with two elements: 1) high or low CNC flowrate and 2) 1/4 or 1 inch final collimating aperture before chamber one (see Figure 1). Variation of the CNC flowrate was used to examine the influence of mixing on the concentration history. Changing the collimating aperture width varied the initial concentrations in the sample chambers, with the 1 inch aperture admitting a greater number of primary droplets into the chamber, which results in significantly higher initial concentrations and larger mean particle sizes than with the 1/4 inch aperture. In all, twelve concentration history measurements were made with the CNC.

2.2 PRINCIPLE OF OPERATION

The CNC used in this study (Model 3022, TSI Inc., St. Paul, MN) continuously samples and counts particles by enlarging them to a size that can be detected easily. Particles larger than 0.01 μm are grown in a supersaturated butanol environment to a size large enough to be counted by light scattering methods. The concentration range that can be measured is from less than 0.01 particles/cm^3 to 1x10^7 particles/cm^3. For concentrations up to 10,000 particles/cm^3 the instrument operates in single-count mode, where the individual light scattering pulses from each droplet are counted; this mode does not require calibration. Above 10,000 particles/cm^3, the concentration is determined from the ensemble light scattered by all of the droplets in the sensing volume; this range requires a calibration (performed at the factory and not verified at Sandia for this work) to establish the relationship between scattering intensity and concentration. Two sample flowrates are available: a low flowrate (0.268 liters/minute) and a high flowrate (1.32 liters/minute).

2.3 ANALYSIS

To consider the concentration decay, a simple model is proposed here. For a monodisperse aerosol, the rate of loss of particles from a chamber is given by (Hinds, 1982):

$$\frac{dN}{dt} = -KN^2 - \alpha N \tag{1}$$

where N is the particle concentration (#/cm^3), K is the coagulation coefficient (cm^3/minute), and α is a linear loss rate (min^{-1}). The linear loss rate can primarily result from two sources: losses to the surfaces of the chamber and losses resulting from withdrawing aerosol from the chamber for measurement (the makeup air is filtered so that the flow entering the chamber contains no particles). Neglecting wall losses, the sampling loss coefficient can be calculated from the chamber volume V and the sampled flowrate Q as $\alpha=Q/V$. A closed form solution for the above equation is:

$$N = \frac{\alpha}{\frac{KN_o + \alpha}{N_o} e^{\alpha t} - K} \tag{2}$$

where N_o is the initial concentration. The difficulty in applying Equations (1) and (2) in the present study is that they strictly apply only for a monodisperse aerosol, whereas the actual aerosol size distribution is approximately lognormal and is changing with time. However, Hinds (1982) shows that for pure coagulation of lognormal aerosols (as the present combustion aerosol are shown to be in Chapters 3 and 4) it is possible to reasonably approximate the concentration decay using an equation analogous to Equation (1) with an average coagulation coefficient that changes slowly with time. Thus, as a rough approximation, the simple analysis presented above will be applied to the present data.

Two sets of data are analyzed below. First, late-time concentration decay measurements are reported for which linear loss mechanisms dominate coagulation and an exponential decay is observed. Second, early-time measurements show the importance of coagulation.

2.4 LATE-TIME CONCENTRATION DECAY

In the first set of tests, the aerosol in the chamber was sampled at late time (hours after the launch) for which concentrations are low and coagulation can be neglected. Tests were made at both the low and high flowrates (0.268 and 1.32 LPM) and are shown in Figure 3 as concentration vs. elapsed time (in this case time is counted beginning with start of the measurements, long after the initial launch). The data marked URAN.121B were taken at the low flowrate beginning about 23 hours after the launch, while the data marked URAN.122C were taken at the high flowrate beginning about 6 hours after launch. Clearly the concentration decays much more rapidly for the high flowrate test than for the low flowrate.

To quantify the results, a least squares minimization using Equation (2) was used to find the best-fit for the loss rate α neglecting coagulation (K=0) and assuming a slowly varying size distribution. Under these assumptions, the concentration should decay exponentially (for a well-mixed chamber), with a decay constant resulting from both wall losses and sampling losses. The best-fit curves are also shown in Figure 3, and are seen to provide a good description of the observations. Fluctuations about the fit are typically less than 10% for the high flowrate test, and less than 15% for the low flowrate test (although one 30% deviation was observed). An interesting comparison is between the best-fit values for α and the value calculated neglecting wall losses, for which the decay constant is the ratio of the CNC flowrate to the total volume being sampled from (48.6 liters). The calculated values of α for the low and high CNC flowrates, 0.00551 and 0.0272 min^{-1} respectively, are in excellent agreement with the fitted values of 0.00552 and 0.0273, respectively. This agreement suggests that in late time the decrease in particle concentration is dominated by sampling rather than by wall losses or coagulation. Interestingly, although wall losses can be neglected when considering number loss, it will be shown later that wall losses can be important when considering mass loss. Finally, when sampling losses dominate, α does not depend explicitly on the aerosol size distribution and is truly a constant.

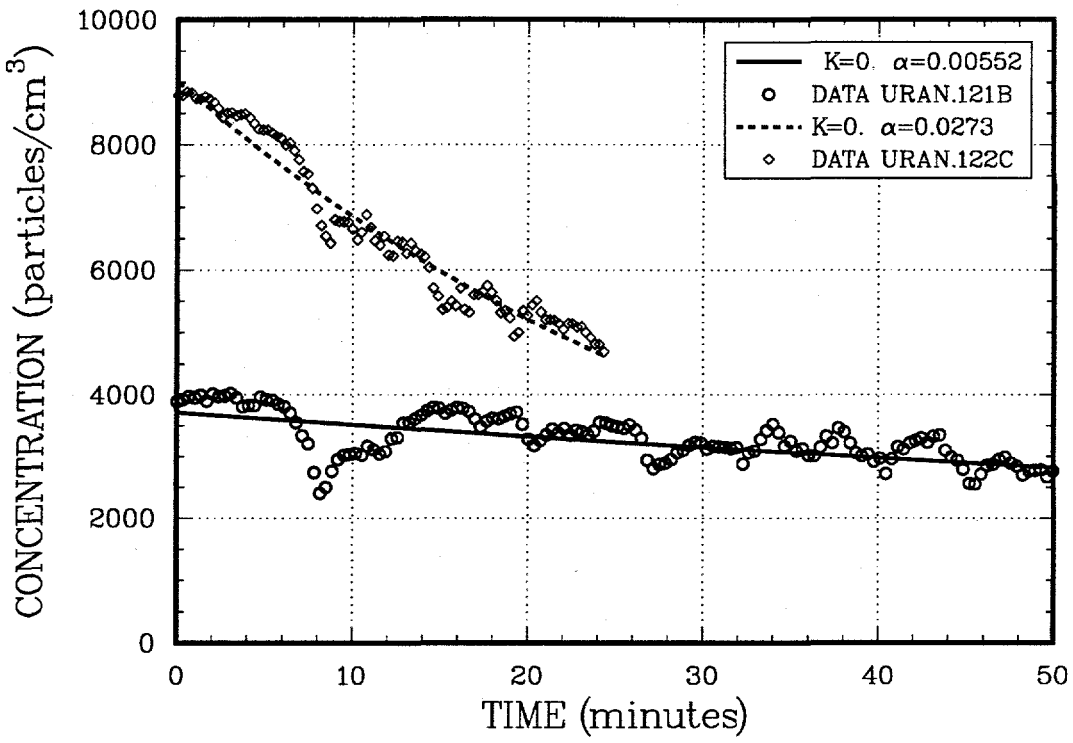

Figure 3. Comparison of high and low CNC flowrate concentration histories (late time).

2.5 EARLY-TIME CONCENTRATION DECAY

This section reports results from CNC measurements designed to explore the concentration decay immediately after launch. Initially, the concentration will be higher and the particle size smaller than at any other time during the test; both of these conditions favor coagulation as the mechanism controlling the evolution of the size distribution. Tests were made with both the large (1 inch) and small (1/4 inch) apertures, always at the high CNC flowrate.

2.5.1 Large-Aperture Results

Two tests at the high CNC flowrate (URAN.128 and URAN.129) were made using the wide (1 inch) aperture; the concentration histories for these tests are shown in Figure 4. These tests are reasonably consistent, and show a monotonic decrease with fairly limited fluctuations. The decline in concentration is significantly more rapid than the late-time results shown in Figure 3, and results from coagulation at these high concentrations. A least squares minimization of Equation (2) was used to find the best-fit for the coagulation coefficient K (assuming α to be a constant equal to the sampling loss rate, 0.0272 min^{-1}). The resulting values of K=1.3x10^{-7} and 1.0x10^{-7} cm^3/min for URAN.128 and URAN.129, respectively, are in reasonable agreement; Figure 4 also shows reasonable agreement between the data and the best-fit curve.

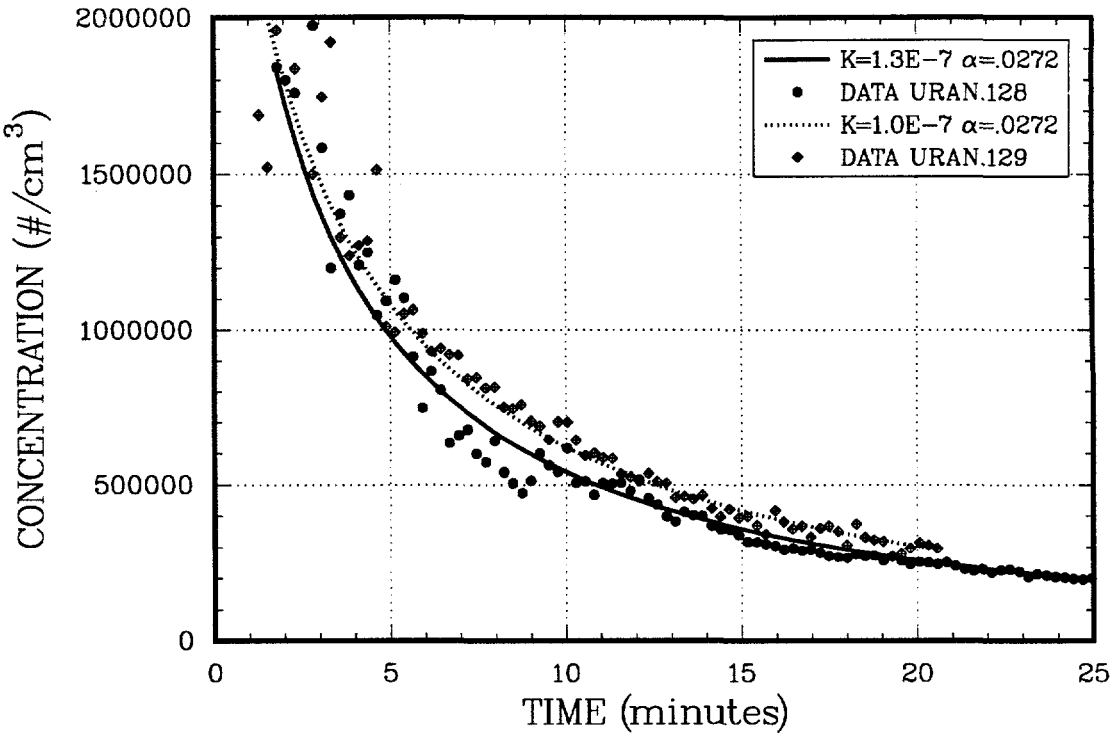

Figure 4. Concentration decay for large (1 inch) aperture tests at high flowrates.

As mentioned previously, the use of an average coagulation coefficient is only approximate. Since an accurate model must account for the coagulation of each particle with particles of every other size (Hinds, 1982), the true coagulation rate depends on the particle size distribution. In addition, the size distribution itself (and thus the average coagulation coefficient) is changing with time as a result of coagulation. As stated above, Hinds (1982) suggests that the coagulation rate of a lognormal distribution can be approximated with Equation (1) using an average coagulation coefficient that changes slowly with time, and he presents a table (Hinds, 1982, p.243) summarizing the effective coagulation coefficient for spherical particles as a function of the lognormal count median size (CMD) and geometric standard deviation (GSD). Although the present combustion aerosol is adequately described by a lognormal distribution, the extremely nonspherical nature of the particles will lead to an enhancement in their apparent coagulation rate because of their greater surface compared to an equal-volume sphere (Hinds, 1992, p.240). Thus, it is interesting to compare the observed coagulation constant with that calculated for lognormal distributions of spherical particles.

Size distribution measurements (see Chapter 3) made immediately after these CNC tests give a count median diameter (CMD) of about 0.85 μm and a geometric standard deviation (GSD) of slightly less than 2 for both tests; the corresponding spherical-particle coagulation coefficient $K \cong 3.0 \times 10^{-8}$ cm^3/min (Hinds, 1982, p.243) is about a factor of three smaller than the observed coefficient $K \cong 1.0 \times 10^{-7}$ cm^3/min. Other measurements (see Chapter 3 also) suggest that the initial size distribution (soon after launch) has a

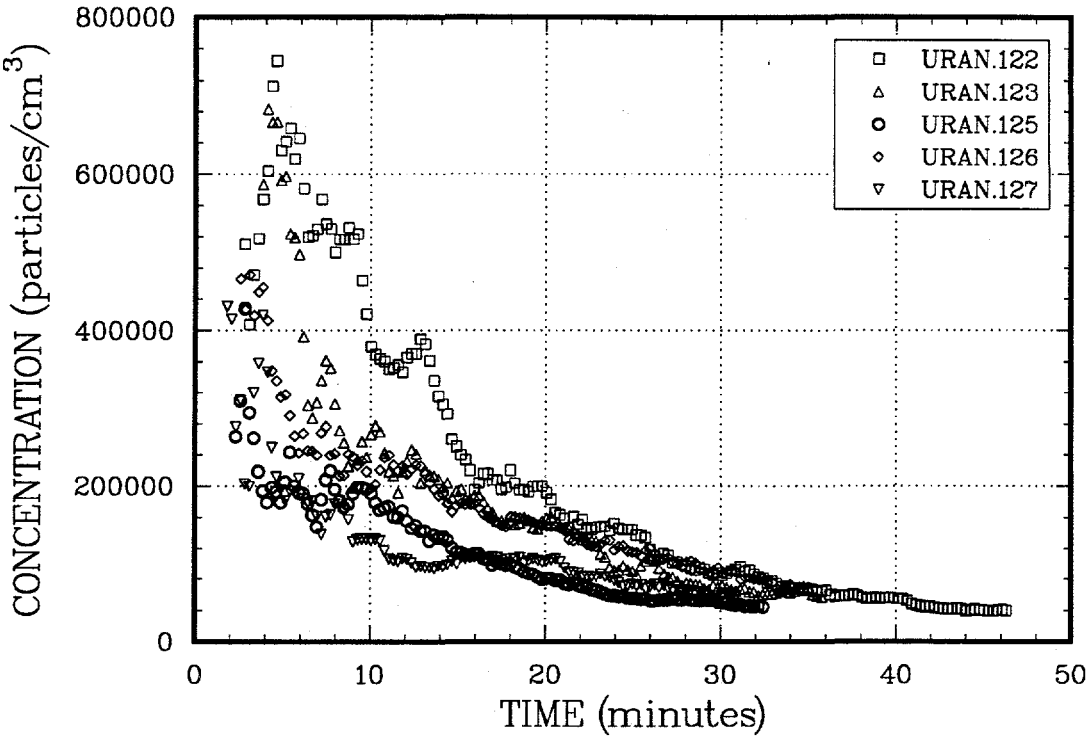

Figure 5. Concentration decay for small (1/4 inch) aperture at high flowrates.

CMD≅0.3 μm and GSD≅2, which gives a spherical-particle coagulation coefficient K≅4.5x10^{-8} cm^3/min that is still a factor of two smaller than the observed K. Thus, nonsphericity results in a significantly higher coagulation rate than would be expected for an equivalent sphere. For comparison, a lognormal distribution of spherical particles with CMD=0.1 μm and GSD=2 would give about the same coagulation rate as is measured, so that the uranium combustion aerosol coagulates at the same rate as a much smaller aerosol. An additional factor which has not been considered (and has not been measured) is the possible distribution of charge among the particles, which can also dramatically change the coagulation rate. In any case, the present estimates of the coagulation rate are the best available.

2.5.2 Small-Aperture Results

Five tests at the higher CNC flowrate with the smaller aperture (1/4 inch) were made; concentration histories for these tests are shown in Figure 5. Two aspects of the results are emphasized here. First, the concentration histories of the five tests show considerable variation, although these tests were made under similar conditions. This lack of repeatability is unexplained, although the use of the narrower aperture is a possibility since the 1 inch aperture tests gave repeatable results (although only two tests were made with the larger aperture). Second, larger fluctuations are observed in the concentration history for each test. The cause of this variation is also not known; it is interesting that the large aperture tests (using the same CNC flowrate) showed significantly less fluctuations,

implying that the flowrate (and hence mixing) is not the problem. Despite the great variability and the fluctuations, a least squares minimization of Equation (2) was used to find the best-fit for the coagulation coefficient K (assuming α to be a constant equal to the sampling loss rate, 0.0272 min^{-1}). The resulting best-fit values for K spanned a fairly broad range, from $1.4x10^{-7}$ to $3.0x10^{-7}$ cm^3/min. Notably, this range exceeds the best-fit value for K found in the large-aperture tests. The apparently larger values for K are at least qualitatively correct: reducing the aperture limits the total amount of material entering the chamber, lowering the initial concentration and ultimately giving an aerosol with a smaller mean diameter. As smaller particles diffuse more rapidly, the effective coagulation rate will be faster for an aerosol with a smaller mean diameter. Size distribution measurements made after the CNC samples confirm that smaller particles are generated with the small aperture, with measured CMDs of between 0.5 and 0.75 μm (compared to 0.85 μm for the large-aperture tests). The distributions were also slightly wider than for the large aperture tests, with geometric standard deviations of between 1.9 and 2. However, due to the great variability observed in these tests, a quantitative analysis is not warranted.

2.6 CONCLUSIONS

The above concentration measurements provide several valuable insights into the dynamics of this combustion-generated aerosol. Most important is that the concentration is not constant, but decays with time as a result of coagulation, sampling losses, and wall losses. The most rapid decay is seen immediately after launch, when the combination of small particle size and high concentration leads to rapid coagulation. Despite the variability in the data, an attempt was made to describe the dynamics of the concentration decay with a simple model that includes coagulation, wall losses, and sampling losses. The model strictly applies only for monodisperse aerosol, so the resulting best-fit parameters are averaged over both the particle size distribution and time. Immediately after launch, coagulation dominates other particle loss mechanisms. For the large aperture tests, the best-fit coagulation coefficient during the first 15 minutes is $K \cong 1x10^{-7}$ cm^3/min. Tests using a smaller aperture show greater variability, giving best-fit coagulation coefficients in the range from $1.4x10^{-7}$ to $3.0x10^{-7}$ cm^3/min. These values are two to three times greater than would be expected for spheres with the same measured size (typically between 0.5 and 1.0 μm). The cause of this enhancement is likely the highly nonspherical, chain-agglomerate structure of the particles. Thus, coagulation rates of similar aerosol in the field may be significantly higher than expected based on measured size distributions.

A second interesting result is that the late-time concentration decay is well-described by a simple model that includes only sampling losses. Thus, both wall losses and coagulation can be neglected for late-time concentration decay. Tests at both high and low sample flowrates were performed and the observed particle concentration decay could be well described by the model. Although concentration losses (number of particles) to the chamber walls are generally small, the impactor measurements of Chapter 4 will show that mass losses to the walls by settling cannot be neglected. This apparent difference results from the fact that the largest particles are preferentially being lost by sedimentation, so that a small number of particles represent a disproportionately large fraction of the total suspended mass.

3.0 DIFFERENTIAL MOBILITY PARTICLE SIZER

3.1 INTRODUCTION

This chapter describes tests using a Differential Mobility Particle Sizer (DMPS) to measure the number distribution (based on electric mobility equivalent diameter, d_{me}) of launcher-generated aerosol. The electric mobility and mobility equivalent diameters are equal if orientation effects are neglected; the latter is the appropriate characteristic diameter for predicting particle coagulation and diffusion rates. Due to the high resolution of the DMPS technique, many tests were conducted to look at the time evolution of the size distribution. As seen previously, the number concentration decays rapidly immediately after the launch due to coagulation; by conservation of mass, the remaining particles must be growing in size. One goal of this series of tests is to explore the growth in particle size and to correlate it with the observed decrease in concentration. Comparisons of the DMPS and CNC results are also presented in this chapter.

3.2 PRINCIPLE OF OPERATION

The DMPS has been used previously to measure the size distribution of combustion aerosol generated by the launch of high-velocity molten-metal droplets of zirconium and tungsten (Rader and Benson, 1988). A complete description of the principle of operation of the DMPS and subsequent data analysis techniques are found in that report. A brief review of the DMPS principle of operation is presented in this section. In Appendix B, recent improvements in the data reduction scheme are reported.

The DMPS consists of two subsystems: an Electrostatic Classifier (EC)(Model 3071, TSI, Inc., St. Paul, MN) and a Condensation Nucleus Counter (CNC)(Model 3022 discussed above). In the broadest terms, the EC samples the aerosol of interest, charges the particles with a bipolar ion source, and selects (classifies) from the overall distribution only those charged particles within a narrow band of electric mobilities (particle sizes). The electric mobility band selected by the EC is controlled by four flowrates (aerosol sample and monodisperse flows both equal to 0.268 lpm, and sheath inlet and outlet flows both equal to 3.43 lpm) and the applied classification voltage (0 to -10,000 volts DC). The selected particles exit the EC and are counted by the CNC. A size distribution is built up by scanning the EC over a range of electric mobilities (by varying the classification voltage) and measuring the concentration at each mobility with the CNC. An example of the raw data recorded by the DMPS is shown in Figure 6, which shows the measured CNC concentration in particles/cm^3 as a function of the applied classification voltage. A single size distribution measurement takes about 6 minutes to complete.

An important feature of the DMPS is that it actually measures an electric mobility distribution, from which the actual size distribution is inferred. The inversion is complicated by the fact that a particle's electric mobility depends on its size, shape, orientation, and the number of charges it carries. Thus, the inversion process needs to include accurate models for: (1) converting between electric mobility and equivalent mobility diameter, (2) calculating the charge distribution of the aerosol exiting the bipolar

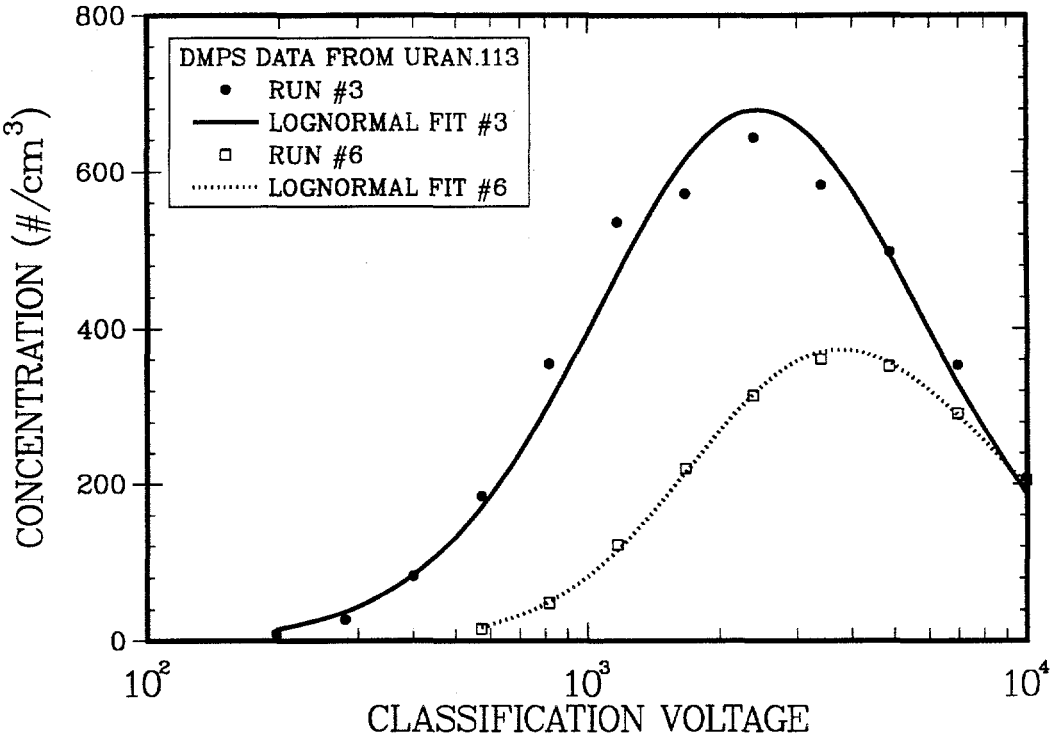

Figure 6. Comparison of best-fit and raw data from two DMPS measurement.

ion source, (3) predicting the classification properties of the EC (based on its geometry, flowrates, and applied voltage), and (4) a functional form for the unknown size distribution. In this work, as discussed in Appendix B, only the charging law has been changed from the method described in Rader and Benson (1988). As in earlier studies, the combustion aerosol is assumed to be lognormal and so characterized by three parameters: N_T the total particle number concentration, CMD the count median mobility equivalent diameter, and σ_g the geometric standard deviation based on the mobility equivalent diameter. With the lognormal assumption, the determination of the number distribution reduces to the problem of finding the three parameters, N_T, CMD, and σ_g, that best describe the observed DMPS measurements (see Appendix B for details).

The effect of particle shape on DMPS measurements is also critical for the present work, which features highly branched chain agglomerates. The particles in the EC are actually sorted by a balance between the electrical force (proportional to the number of charges on the particle) acting to accelerate the particle and a drag force proportional to velocity that acts to restrain the motion. The DMPS actually reports an *electric mobility equivalent diameter*, d_{me}, which is the diameter of a sphere that moves with the same velocity as the particle of interest under the same electrical force. For the nonspherical particles of this study, the relationship between the electric mobility equivalent diameter and some characteristic length scale of the particle (such as observed under SEM) is not obvious. In addition, nonspherical particles can show alignment effects where particular orientations

are favored during the separation process. Under the assumption that the particles are fractal-like, however, it is known that the mobility diameter and the radius of gyration (a measure of the apparent size of a particle deduced from an image of it) are linearly related. Also, a reasonable assumption is that because of their random structure, there is no preferential orientation during separation in the DMPS, so that the electric mobility diameter can be equated with the mobility diameter. The value of the mobility diameter is the appropriate diameter to use to characterize particle coagulation or diffusional transport.

3.3 DATA ACQUISITION/INVERSION CHECKS

One of the checks of the validity of the assumptions of Appendix B (especially the lognormal distribution and the charging law) is the agreement between the best-fit predictions and the observed data. Two such comparisons are shown in Figure 6 for a representative test (URAN.113). Run #3 is an early-time result (about 20 minutes after launch) while Run #6 is a late-time result (about 3 hours after launch). Although the agreement between the fit and data is excellent for Run #6, there are significant discrepancies between the fit and data for Run #3. This pattern is consistent throughout all of the DMPS data, with late-time fits being quite good while early-fits are less acceptable. Two main explanations for this behavior are offered. First, as observed in the direct CNC measurements of the previous chapter, there are dramatic fluctuations in the concentration at early times. Again, these fluctuations likely result from insufficient mixing within the chamber. These fluctuations are reflected in DMPS measurements, which require about six to ten minutes to complete an entire size scan such as shown in Figure 6. A second source of difficulty is that the initial concentrations lead to rapid concentration decay due to coagulation. Again, since the DMPS requires about six minutes to complete a size scan, the size distribution will change during the measurement so that the sampled aerosol at the first and last voltage can be appreciably different. This latter effect can be reduced by not weighting the least-squares sum, thereby emphasizing the high-concentrations near the peak that are more closely clustered in time.[1] For these reasons, uncertainties in the early-time fits are much greater than for late-time fits.

A second check of the entire fitting algorithm is to compare the total concentration resulting from the DMPS inversion algorithm, N_T, with a direct concentration measurement made with the CNC. Many such comparisons were made for a variety of conditions and these results are shown in Figure 7. The agreement between the direct measurement and the DMPS best-fit is excellent for the lower concentrations, but the differences become significant at the higher concentrations. As discussed before, the high concentration DMPS measurements are less reliable, so the observed increase in scatter in this range is expected. In general, it appears that there is no systematic difference between the DMPS and CNC results. This good agreement offers support for all of the assumptions that have led to present DMPS inversion algorithm (including the use of different weightings in data inversion for high and low concentrations). It is interesting to note that the Boltzmann-Gunn charging mechanism used in the previous studies (Rader and Benson, 1988) would

1. The statistical weighting, however, was used in fitting Run #3 to show the worst case. In addition, Run #3 was among the poorer fits obtained in this study, and was selected to show the worst case.

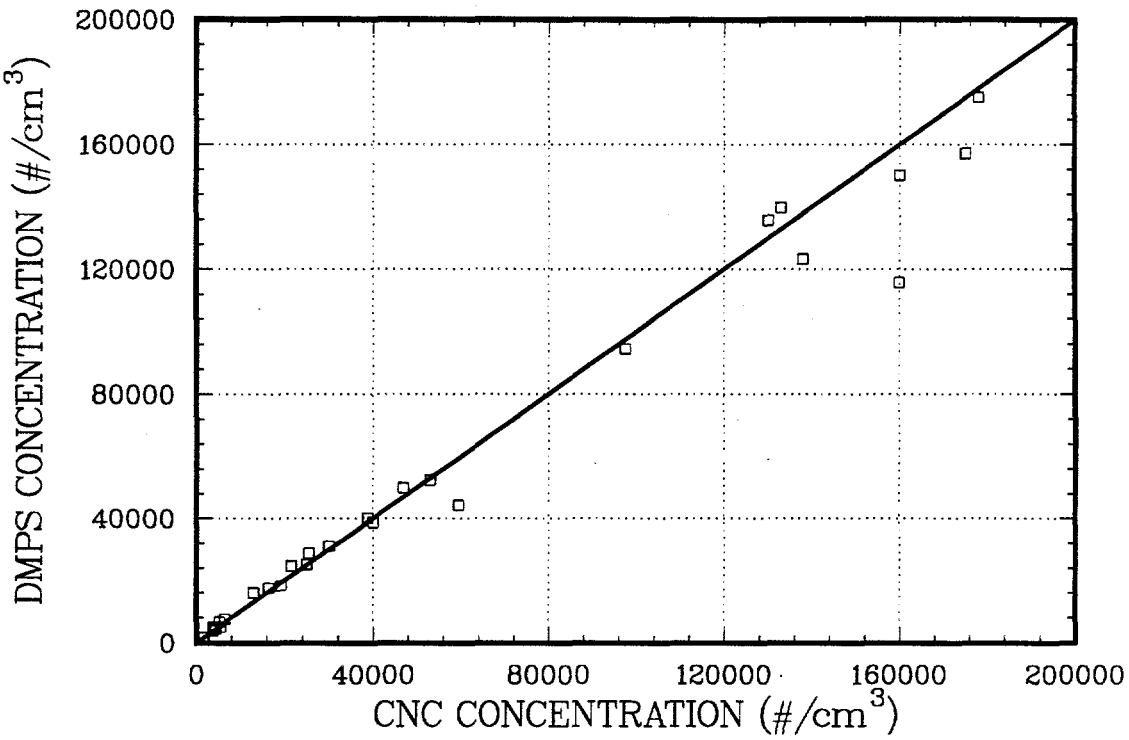

Figure 7. Comparison between total concentration measured directly by the CNC and from the inversion of DMPS mobility distribution data.

not provide the same degree of correlation as the present method (see Appendix B), since it gives DMPS concentrations 30 to 50% lower than the present method.

3.4 DMPS RESULTS

3.4.1 Initial Size Distribution

One of the key questions regarding the combustion-generated aerosol under study is its initial size distribution. Unfortunately, this distribution is impossible to measure with the present experimental setup since the aerosol is initially concentrated in a very small volume associated with the droplet wakes. Presumably high concentrations in this region result in rapid coagulation. At the same time, chamber turbulence and particle diffusion also act to disperse the particles and reduce the local concentration. The first glimpse of the size distribution possible with the DMPS occurs after mixing has spread the aerosol throughout the chamber; the first glimpse is further distorted by the relatively long period required by the DMPS to complete a single size distribution measurement. Even after this initial lag time, as the CNC measurements discussed previously show, concentrations remain high enough that coagulation continues to decrease the number of particles while increasing their mean sizes. With these limitations in mind, this section describes our efforts to measure the "initial" size distribution, which we take here to mean the size distribution of particles that have escaped the wake region.

To aid in analyzing the early time size distribution, one test (URAN.113) was made in which a flow of 10 lpm was withdrawn from the chamber immediately after launch for a period of 5 minutes. The intent of this procedure was to rapidly reduce the aerosol concentration in the chamber and thus inhibit agglomerate growth. After the 5 minutes, the DMPS was used to measure the remaining aerosol.[1] A best fit to the DMPS data gave a total number concentration N_T equal to about 90,000 #/cm^3, a count median diameter (CMD) of 0.33 μm, and a geometric standard deviation σ_g of about 2.0. In a subsequent test (URAN.114), a 15 lpm flowrate was withdrawn from the chamber for 8 minutes; DMPS measurements after this time gave N_T = 45,000 #/cm^3, CMD = 0.27 μm, and σ_g = 1.9. In a final test (URAN.115), a 15 lpm flowrate was withdrawn from the chamber for 10 minutes; DMPS measurements after this time gave N_T = 25,000 #/cm^3, CMD = 0.30 μm, and σ_g = 1.95.

From these tests, our best estimate for the early-time distribution in the chamber is a lognormal distribution having a mobility mean diameter of about 0.3 μm with a geometric standard deviation of about 2.0. As discussed above, this result likely describes the aerosol escaping the wake region left behind the droplets.

3.4.2 Size Distribution Evolution

A second area of interest is the evolution of the size distribution resulting from the combination of coagulation, sampling losses, and wall deposition. To explore these phenomena, DMPS measurements were made at various times after launch. One example is shown in Figure 8, which shows best-fit lognormal distributions for various times after launch on test URAN.113. Over the three hour period shown, the CMD approximately doubles while the total concentration decreases by a factor of over four. This behavior is consistent with early-time behavior in which coagulation is playing a major role in the concentration decay rate. DMPS measurements made 1400 minutes after launch showed a reduction in concentration by an additional factor of four, but with no noticeable change in CMD. The latter behavior is consistent with late-time behavior in which linear loss mechanisms dominate coagulation. Over the entire 1400 minute test, the geometric standard deviation σ_g declined from about 1.95 initially to about 1.75 at the end of the test.

The decrease in σ_g with time is primarily the result of coagulation, which is known to reduce the spread of the distribution (as measured by σ_g) with time. Physically, the narrowing of the distribution arises as the coagulation rate between two size classes of particles increases as the size difference between the two size classes increases. Thus, particles at the opposing tails of the distribution will be preferentially diminished. Tests performed at higher initial concentrations show even greater changes in σ_g, since coagulation is more pronounced. For example, test URAN.112 started with an initial concentration of about 230,000 #/cm^3 and showed a decrease in σ_g from about 2.25 initially to about 1.78 after about three hours.

---

1. Note that although the 50 lpm withdrawn exceeds the chamber volume, many particles remain in the chamber as the sampling process results in a mixing-type exponential decay in particle number.

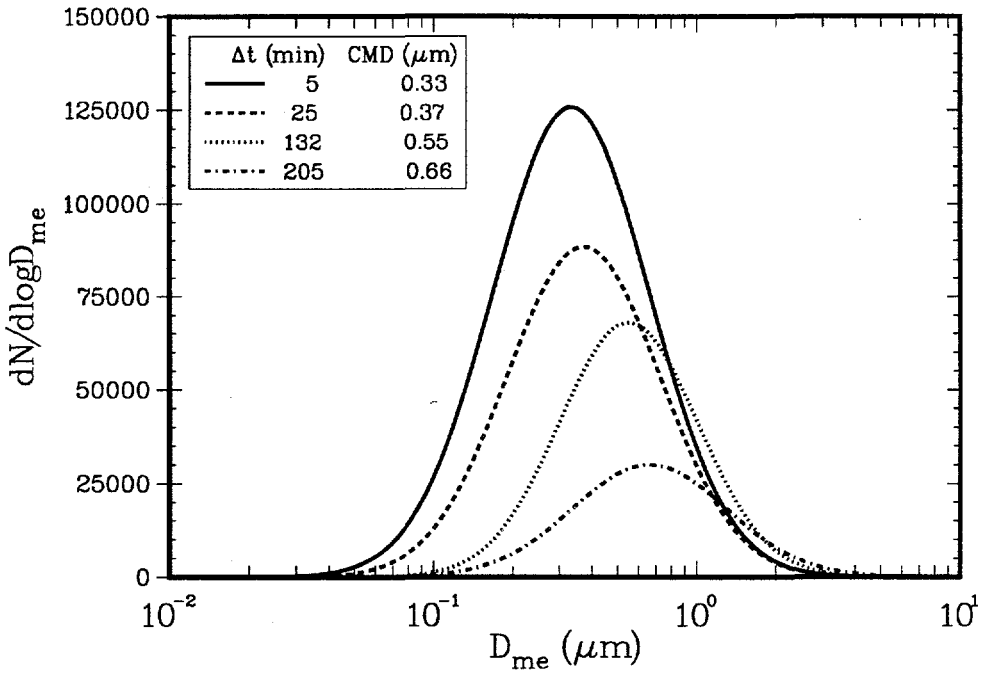

Figure 8. Time evolution of aerosol distribution from URAN.113.

3.5 CONCLUSIONS

The present DMPS tests supported several earlier observations and also provided new results. As shown for other metals, the agglomerates generated by the high-velocity combustion of uranium alloy droplets can be adequately described by a simple lognormal distribution. The size distributions are very similar to those observed for earlier tests with tungsten: both give early-time CMDs of 0.3 - 0.4 μm with geometric standard deviations of about 2. The concentrations observed in the current uranium tests, however, were at least two orders of magnitude greater than in the earlier tungsten tests, possibly resulting from the more energetic combustion of uranium. The distributions observed for earlier zirconium tests showed similar mean sizes, but much broader distributions than at present. The spread in the distribution may be a result of the sparking phenomena observed in zirconium combustion that is not observed in either tungsten or uranium combustion.

A major advance in the present work was the use of a new charging algorithm, which greatly improved the agreement between DMPS best-fit predictions and CNC direct measurements of the total concentration. As expected, DMPS measurements confirm that the size distribution falls in number, grows in size, and narrows in spread when coagulation is active.

4.0 MICROORIFICE UNIFORM DEPOSIT IMPACTOR

4.1 INTRODUCTION

The intent of the impactor tests presented below was to measure the mass aerodynamic size distribution of launcher-generated aerosol using the Microorifice Uniform Deposit Impactor (MOUDI). The aerodynamic diameter, d_{ae}, is of interest as it is the appropriate diameter to use in calculations of particle sedimentation rates and in assessing particle transport efficiencies - such as through the lung during respiration or through sampling systems. The mass distribution is also of interest since it is frequently measured in the field and is required in trying to infer the original mass of the aerosol source. A limited attempt was made to look at the time evolution of the size distribution by performing early- and late-time MOUDI mass distribution measurements. Most of the MOUDI tests were conducted in conjunction with DMPS and/or CNC measurements. CNC samples were typically drawn directly from the chamber both before and after the MOUDI samples to determine the total concentration of particles. Several analytic techniques are presented in this chapter for comparing impactor mass distributions (based on aerodynamic diameter) with the DMPS number distributions (based on mobility diameter) presented earlier.

4.2 PRINCIPLE OF OPERATION

The Microorifice Uniform Deposit Impactor (MSP Corp., Minneapolis, MN) is a multistage cascade impactor capable of separating an aerosol sample into eight size bins with aerodynamic diameters between 0.056 and 18 μm at a flow rate of 30 liters/minute. A complete description of the instrument, along with a calibration and recommendations for proper use has been recently reported (Marple, Rubow, and Behm, 1991). Basically, an impactor achieves size-selective particle collection by directing a jet of particle-laden air at a flat plate. Large particles are unable to follow the fluid as it changes direction and impact on the plate, while small particles follow the airflow and are not collected. Ideally, there is some characteristic size above which collection is 100%, and below which all particles pass through. In practice, the stage response (collection efficiency vs. particle size) is not a step function, but increases monotonically from 0 to 100% collection over a finite range of particle size. A sharp response function can be obtained, however, with careful impactor design. For inertial impaction, the characteristic particle size turns out to be its aerodynamic diameter (the diameter of a sphere with the density of water that falls under gravity at the same speed as the particle of interest). After operating the impactor for a given length of time, the collection plate can be removed and analyzed (gravimetrically, for example) to determine the mass of particles collected. Particle concentration (suspended particle mass per unit volume of air) can be calculated from the flow rate, sample time, and the measured mass.

A cascade impactor, such as the MOUDI, passes the aerosol through a series of stages with different characteristic cut-sizes to separate the particles into discrete size ranges. Smaller cut-sizes are obtained at each stage by using progressively smaller nozzle diameters to give higher jet velocities. Single stage performance for spherical particles is controlled by the

Stokes number, a dimensionless particle size which measures the particles' ability to follow changes in fluid streamlines:

$$St = \frac{\rho_p C(d_p) V_o d_p^2}{18\mu W} \tag{3}$$

where d_p and ρ_p are the particle physical diameter and density (assuming a sphere), V_o is the average air velocity through the nozzle (volume flow rate/nozzle area), μ is the gas viscosity, and W is the nozzle diameter. $C(d_p)$ is the particle slip correction factor, which depends on particle diameter and certain gas properties. For spherical particles in air, the slip correction factor can be approximated as:

$$C \approx 1 + \frac{0.163}{d_p(\mu m)} \frac{P_o}{P} \tag{4}$$

where P_o and P are the standard (760 mm Hg) and local pressures (within the MOUDI), respectively. Equation (4) is reasonably accurate for temperatures near 23°C and for particles larger than about 0.5 μm (for smaller particles, see Rader, 1990).

As the collection performance of a single stage is actually a function of St (and hence d_p), it is convenient to introduce 50% cut-point quantities, such as d_{p50} which is the diameter for which 50% of the particles are collected on the stage. Equation (3) can be rearranged to give the following expression for d_{p50} for spherical particles:

$$d_{p50} = \sqrt{\frac{9\mu W}{\rho_p C(d_{p50}) V_o}} \sqrt{St_{50}} \,. \tag{5}$$

For a given impactor geometry over a wide range of Reynolds number, St_{50} is a constant. Thus, decreasing the nozzle diameter or increasing the jet velocity reduces the particle cut-point diameter that is collected by the stage.

Note that the particle-dependent part of St (see Equation 3) turns out to be related to the square of the aerodynamic diameter (d_{ae}) mentioned above, which is defined for spherical particles as (Hinds, 1982: p. 49):

$$\sqrt{C(d_{ae})} \cdot d_{ae} = \sqrt{\rho_p C(d_p)} \cdot d_p \,. \tag{6}$$

Most frequently, the cut-off diameters and performance characteristics of an impactor are reported in terms of aerodynamic diameter; consequently, size distributions measured with an impactor are typically reported in terms of aerodynamic diameter. For spherical particles, the aerodynamic cut-point diameter can be obtained from Equations (5) and (6).

The MOUDI offers several novel features. First, the ability to collect particles as small as 0.056 μm is accomplished through the use of microorifice stages (with holes as small as 52 μm in diameter for the final stage), which are made by a chemical etching process for the smallest diameter nozzles. Second, multiple nozzles (up to 2000 for the final stage) are used to achieve a moderate total pressure drop through the impactor. Third, the stages can be

rotated independently to achieve uniform deposits on the collection substrate (minimizing particle bounce effects). Although a mechanical system is available to rotate the stages, the impactor used in this study was not so equipped and so rotation was accomplished manually. Finally, the stages are interchangeable, so that a set of size-cuts can be selected that are appropriate for the problem. Ten stages are available with the system, but only eight can be used at one time. By placing a collection plate on top of the first stage, the inlet tube can be used to provide a ninth stage (although its cut-point calibration is not as accurate as the others). An after-filter collects all the particles exiting the final stage. Table 1 summarizes the characteristics of the MOUDI impactor stages used in the present study. Since the ambient pressure in Albuquerque is less than one atmosphere (for which the MOUDI was calibrated), a corrected cut-point diameter was used when reducing data taken for this study (see Appendix C for further discussion).

Table 1: Summary of MOUDI stages used in present study (from Marple et al., 1991).

Stage	Nominal Cut-point (μm)	Corrected Cut-point (μm)	Number of Nozzles	Nozzle Diameter (cm)	P/P_o
Inlet	18	18	1	1.71	1.00
3	3.2	3.2	10	0.247	1.00
4	1.8	1.8	20	0.137	1.00
5	1.0	0.99	40	0.072	0.99
6	0.56	0.55	80	0.040	0.97
7	0.32	0.31	900	0.0140	0.95
8	0.173	0.161	900	0.0090	0.89
A	0.099	0.089	2000	0.0055	0.76
B	0.056	0.049	2000	0.0052	0.53
After filter	0.00	0.00	-	-	-

4.3 DATA ANALYSIS

In this study, the particles collected within the MOUDI impacted on thin aluminum-foil discs. To reduce particle bounce, the substrates were sprayed with a silicon spray (Stock No. 11025, Cling Surface Co., Orchard Park, NY) and baked for 90 minutes at 65°C, as suggested by Marple et al. (1991). A 37-mm diameter Gelman glass fiber after-filter was used, with particle retention rate well above 99%. After sampling, the weight of particles collected on the foils and filter was determined with a Sartorius balance (Model R160P, Sartorius Inc., Bohemia, NY). The gravimetric precision was estimated to be about ±0.04 mg for both the foils and filter.

For each MOUDI sample in the present configuration, the data consist of a set of ten weights - one for each of the nine stages (inlet, 3-8, A, and B) and one for the after-filter. From these weights, the particle mass distribution is sought. One approach to obtaining the size distribution is to assume that all of the mass collected on a stage comes from particles with aerodynamic diameters in the size interval larger than its cut-point size, but smaller than the cut-point size of the previous stage. An approximation to the true aerosol size distribution is plotted as a histogram, where the width of the rectangles represents the logarithmic size interval between cut-points and the height is obtained by dividing the mass collected on the stage by the logarithmic width of the interval ($\Delta M/\Delta log d_{ae}$). With this type of plot, the area of the rectangle equals the mass collected within the interval. An example is shown in Figure 9, where the mass distribution $dM/dlogd_{ae}$ is plotted against the aerodynamic diameter d_{ae}. Note that the units for the ordinate are in milligrams.

To simplify discussion of the data, it is assumed that the *mass* distribution measured by the MOUDI is lognormal in aerodynamic diameter. This assumption is supported by earlier observations that the *number* size distributions measured by the DMPS are lognormal in mobility diameter, although the diameters measured by the two instruments are quite different. A lognormal mass distribution is given by:

$$dM = \frac{M_T}{\sqrt{2\pi}\,\ln\sigma_{ae}} exp\left[-\frac{(\ln d_{ae} - \ln \mathrm{MMAD})^2}{2\,(\ln\sigma_{ae})^2}\right] d\ln d_{ae} \quad . \tag{7}$$

where dM is the mass of particles with diameters between $\ln d_{ae}$ and $\ln d_{ae}+d\ln d_{ae}$, M_T is the total mass sampled, MMAD is the mass median aerodynamic diameter and σ_{ae} is the geometric standard deviation based on aerodynamic diameter.

With the lognormal assumption, the determination of the mass distribution reduces to the problem of finding the three parameters, M_T, MMAD, and σ_{ae}, that best describe the ten measured stage weights. To find these parameters a nonlinear least-squares minimization method (Bevington, 1969) is used in which Equation (7) is integrated (with assumed initial values for the parameters M_T, MMAD, and σ_{ae}) between the appropriate cut-point diameters for each stage, yielding a fitted value for the weight on each stage. The minimization then seeks the values of the three parameters that minimize the sum of squared differences between the predicted and observed weights. No weighting of the differences was used for the impactor (MODE=0).

4.4 RESULTS FROM MOUDI TESTS

For all of the MOUDI tests, the shutter between chambers 2 and 3 was disabled; by combining both chambers it was possible to collect enough aerosol to allow reliable weighing. The three apertures used to collimate the launched material were set at 0.75, 1., and 1. inches (from launcher to sample chambers).

Two basic types of experiments were conducted with the MOUDI to explore the time evolution of the aerosol distribution. To characterize the early-time size distribution two tests, URAN.135 and URAN.136, were made in which a five minute wait after the shot (no

sampling from the chamber) preceded the MOUDI sample. For URAN.135, air from the chamber was sampled for 10 minutes after which the concentration in the chamber was measured by the CNC to be 3800 #/cm^3 (small compared to typical initial concentrations which are of the order of 10^6 #/cm^3). For URAN.136, the five minute wait was followed by only a 5 minute MOUDI sample. In this case, the concentration in the chambers decreased from about 10^6 to 40,000 #/cm^3. Although only about 4% of the total mass was left suspended in the chamber, the remaining concentration was sufficiently high to allow DMPS size distribution measurements. Figure 9 and shows the mass distribution histograms for URAN.135 and URAN.136, respectively. The least-squares method discussed previously was used (without weighting of the differences) to find the best-fit lognormal distribution for each of the tests. These fits are also shown in Figure 9, while the values of the fitted parameters are listed in Table 2. The three fitted parameters for the two tests are in very good agreement. In addition, the fitted values $M_{T,fit}$ are in good agreement with the total mass collected ($M_{T,actual}$ which is the sum of the mass collected on all ten stages), as would be expected if the lognormal assumption is suitable. Thus, based on these two tests, the early-time mass distribution (based on aerodynamic diameter) is characterized by a MMAD of about 0.47 μm with a geometric standard deviation of about 2.3.

To characterize the late-time size distribution two tests, URAN.145 and URAN.150, were made where a 55 minute wait followed the shot (no sampling from the chamber), followed by about 18 minutes of CNC and DMPS measurements, followed by about 6 minutes of sampling through the MOUDI. The fraction of particles remaining in the chamber after the MOUDI sample was measured by the CNC to be about 5% and 2% for URAN.145 and URAN.150, respectively. The mass distribution histograms for URAN.145 and URAN.150 are shown in Figure 10. The least-squares method was again used to find the best-fit lognormal distribution for each of the tests. These fits are shown in Figure 10 as well, while the values of the fitted parameters are listed in Table 2. The three fitted parameters for the two tests are in very good agreement. In addition, the fitted values $M_{T,fit}$ are in good agreement with the total mass collected $M_{T,actual}$. Thus, based on these two tests, the late-time mass distribution (based on aerodynamic diameter) is characterized by a MMAD of about 0.63 μm with a geometric standard deviation of about 2.0.

Two additional MOUDI tests were made which were of dubious quality. URAN.147 followed the long-wait protocol, but suffered a partial plug of the MOUDI about 4 minutes into the sampling period. The total mass collected for this test was significantly greater (29%), the mass median diameter was slightly larger (6%), and the geometric standard deviation was essentially the same compared to the other two long-wait tests (URAN.145 and URAN.150). It is not certain whether plugging could have led to these variations. The CNC and DMPS data collected for this test, however, are valid. URAN.144 also followed the long-wait protocol, but in this case the sampling chambers were accidently not cleared after a previous test using nitrogen. Thus, aerosol generated from the previous test as well as some residual nitrogen were present for the launch. In this case, the fitted values for M_T, MMAD, and σ_{ae} were all significantly less (19%, 15%, and 14%, respectively) than for URAN.145 and URAN.150. These observations are qualitatively consistent with the significant reduction in aerosol mass and size expected in tests performed in nitrogen - for which combustion would be dramatically reduced relative to tests in air.

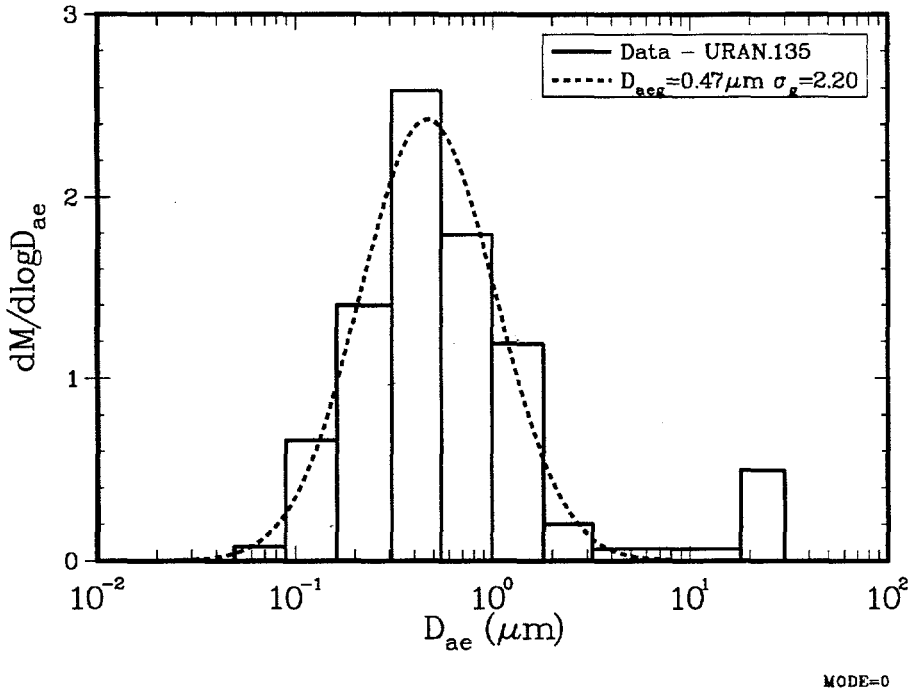

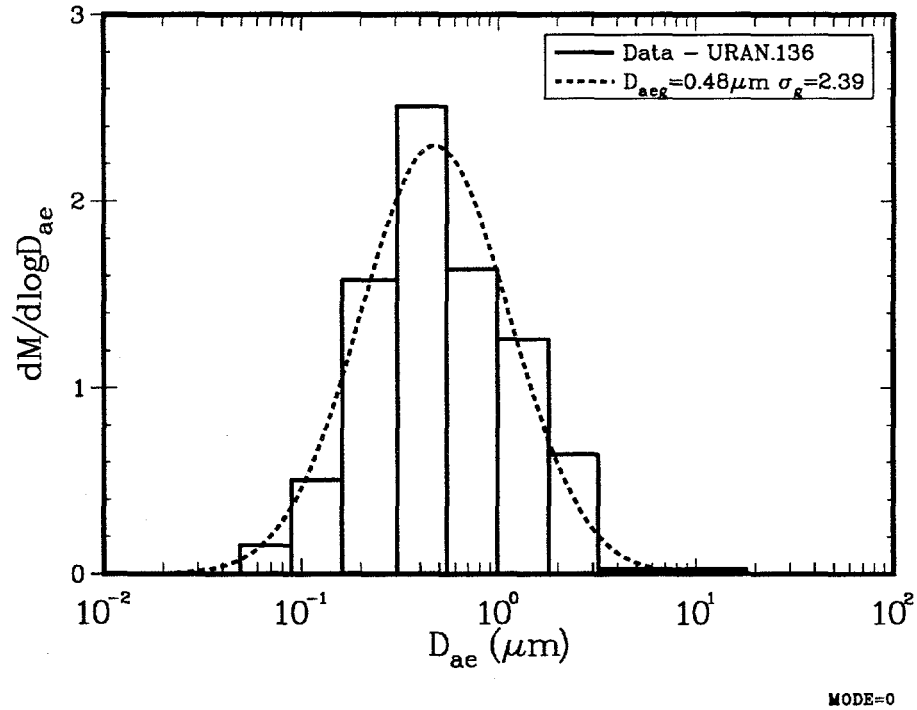

Figure 9. Histogram and lognormal best-fit for early-time MOUDI data for tests URAN.135 and URAN.136.

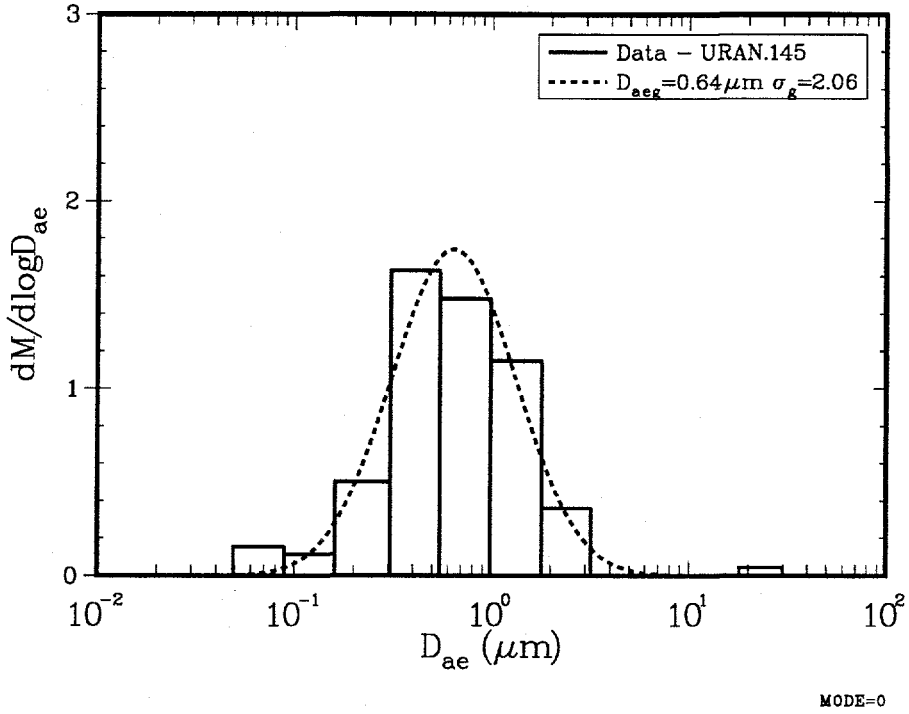

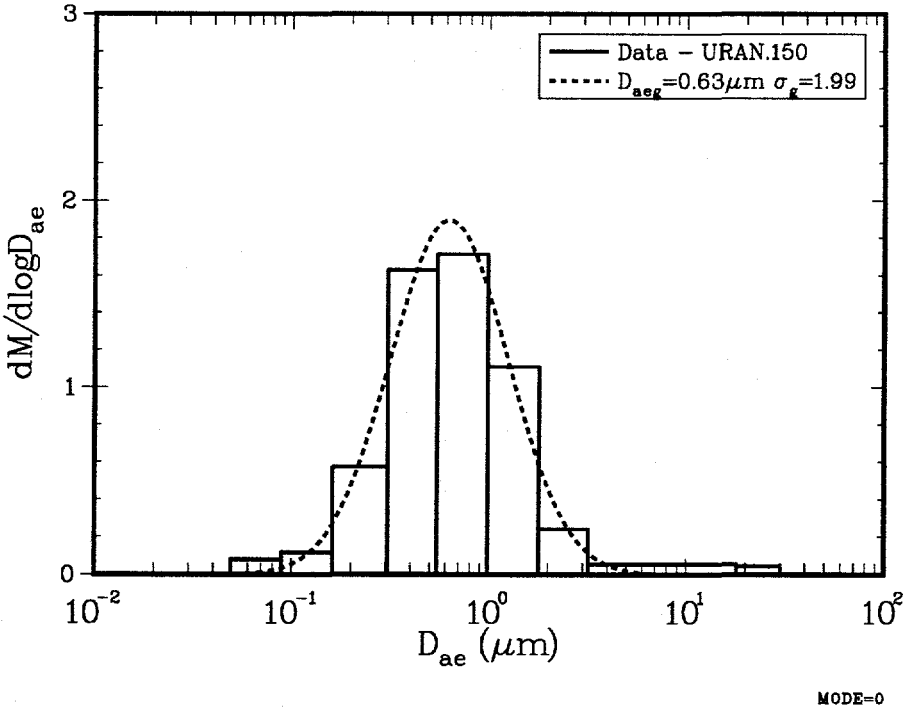

Figure 10. Histogram and lognormal best-fit for late-time MOUDI data on tests URAN.145 and URAN.150.

Table 2: Summary of lognormal fitted parameters for MOUDI experiments.

Run ID URAN	$M_{T,actual}$ (mg)	$M_{T,fit}$ (mg)	MMAD (μm)	σ_{ae} (-)	Comments
135	2.23	2.08	0.468	2.20	early-time
136	2.17	2.18	0.476	2.39	early-time
145	1.40	1.37	0.639	2.06	late-time
150	1.46	1.42	0.627	1.99	late-time
144	1.16	1.00	0.537	1.74	late-time; contaminated
147	1.84	1.81	0.670	1.96	late-time; MOUDI plugged

4.5 COMPARISON WITH DMPS AND CNC TESTS

Most of the MOUDI tests described above were conducted in conjunction with DMPS and/or CNC measurements. CNC samples were typically drawn directly from the chamber both before and after the MOUDI samples to determine the total concentration of particles. The CNC concentrations measured in the chamber immediately before the MOUDI sample is called N_T^{before} and that immediately after the MOUDI sample is called N_T^{after} in Table 3. As can be seen, the total number concentration is about one order of magnitude lower for the late-time distribution (about 72 minutes after launch) than for the early-time distribution (about 5 minutes after launch) as a result of coagulation and/or particle losses. Both the DMPS and CNC results for total concentration are seen to be in excellent agreement if the DMPS best-fit concentration is compared to the appropriate[1] CNC measurement. This agreement is consistent with comparisons of DMPS and CNC concentrations discussed in section 3.3.

Uncertainties in the values for the cut-point diameter and in the weighting method (MODE parameter in Table 3) used in inverting DMPS data (see Appendix B) will result in uncertainties in the fitted values for CMD and σ_g. The fitted value for CMD is most sensitive to the cut-point diameter (for the DMPS preimpactor) for late-time distributions (where the larger median size means a greater fraction of the large-particle tail should be removed by the impactor). To test the sensitivity of the parameters to the assumed cut-point, least-squares fits were made in which the cut-point was assumed to be 2.1 μm (in addition to the standard 4.0 μm choice). For the early-time test (URAN.136) the maximum variations in CMD and σ_g from the standard case were both less than 1%. The influence of

1. For the early-time tests, the DMPS was run after the MOUDI sample so that N_T^{after} must be compared to N_{fit} for URAN.136. For the late-time tests, the DMPS was run before the MOUDI sample so N_T^{before} must be compared with N_{fit} for URAN.145 and URAN.150.

the assumed weighting was also minor for URAN.136. As expected, for the late-time tests (URAN.145, .147, and .150) the effect of cut-point variation becomes more pronounced: the maximum variations in CMD and σ_g from the standard case were each about 10%. Again, the influence of the assumed weighting was much less. These tests help bracket the uncertainties in the DMPS fitted parameters given in Table 3.

Table 3: Comparison of MOUDI, DMPS, and CNC data.

	MOUDI			CNC		DMPS[a]		
Run ID URAN	$M_{T,fit}$ (mg)	MMAD (μm)	σ_{ae} (-)	N_T^{before} (#/cm^3)	N_T^{after} (#/cm^3)	N_{fit} (#/cm^3)	CMD (μm)	σ_g (-)
135	2.07	0.47	2.20	-	$3.8 \cdot 10^3$	-	-	-
136	2.18	0.48	2.39	$1.0 \cdot 10^6$	$4.0 \cdot 10^4$	$3.9 \cdot 10^4$	0.56[b]	1.86
145	1.37	0.64	2.06	$1.3 \cdot 10^5$	$6.7 \cdot 10^3$	$1.4 \cdot 10^5$	0.82[c]	1.79
150	1.42	0.63	1.99	$1.4 \cdot 10^5$	$2.8 \cdot 10^3$	$1.2 \cdot 10^5$	0.93[d]	1.80
147	1.81	0.67	1.96	$1.3 \cdot 10^5$	$8.3 \cdot 10^3$	$1.4 \cdot 10^5$	0.87[e]	1.65

a. D_{max}=4.0 μm
b. Average of three DMPS runs, MODE=-1, after MOUDI sample
c. Average of two DMPS runs, MODE=0, before MOUDI sample
d. Average of two DMPS runs, MODE=0, before MOUDI sample
e. Average of two DMPS runs, MODE=0, before MOUDI sample

When comparing the MOUDI and DMPS results in Table 3, it is essential to consider the fundamental differences between the two techniques: the MOUDI tests provide a *mass* distribution based on *aerodynamic* equivalent diameter while the DMPS provides a *number* distribution based on a *mobility* equivalent diameter. Thus, the fact that the mass median aerodynamic diameter (MMAD) and the count median mobility diameter (CMD) are in reasonably good agreement in Table 3 is disturbing. If the techniques were measuring the same equivalent diameter, then the mass median diameter would be expected to be significantly larger than the count median diameter; instead, the two diameters differ by only a small amount.

The explanation for this apparent paradox lies in how the aerodynamic and mobility equivalent diameters are related for the fractal-like particles being studied here. The following two subsections provide a framework for considering these differences. Two key assumptions are made. First, as supported by both DMPS and MOUDI data, the aerosol size and mass distributions will be approximated by lognormal distributions. Second, the aerosol particles are assumed to be fractal-like, so that the relationship between a particle's characteristic size and its mass, m_p, can be expressed as:

$$m_p = \beta \cdot d_{me}^{D_m} \tag{8}$$

where D_m is the mass fractal number, β is a proportionality constant, and the mobility equivalent diameter d_{me} is taken as the characteristic size. Obviously, for these highly irregular particles, the choice of a characteristic size is important. One established choice is to use the particle's mobility equivalent (or hydrodynamic) diameter in Equation (8) (see Schmidt-Ott et al., 1990). Under the assumption that there is no preferential alignment of particles during sizing by the DMPS, it is the mobility equivalent diameter, d_{me} , that is measured by the DMPS and is used here for the characteristic size in Equation (8). Alternatively, a characteristic size could be determined directly from SEM or TEM photographs of the particles; this approach was not pursued in this work.

The assumption that the particles generated in this study are fractal has not been proven. Although there are techniques for demonstrating the fractal nature of an aerosol sample, the techniques have not been pursued for this work. The present grounds for assuming a fractal structure are qualitative: 1) scanning electron microscope photographs of the particles (see Figure 1) appear similar in nature to those reported in the fractal literature (*e.g.*, Reist et al., 1989), and 2) the coagulation-dominated pathway creating these particles typically results in fractal morphologies (*e.g.*, Witten and Sander, 1981). A careful study of the suitability of a fractal model for these combustion particles is one that should be pursued in the future.

In the absence of a quantified study of the fractal nature of the present aerosol, one question that arises is the appropriate choice of the fractal dimension to be used in the analysis. Cluster-cluster agglomeration is considered the central phenomena controlling the morphology of the present particles, for which numerical kinetic growth simulations give fractal dimensions of 1.95 and 1.80 for the free-molecular and diffusional regimes, respectively (Schaefer and Hurd, 1990). Monomer-cluster agglomeration would result in larger values for the fractal dimension. Thus, in the present work, the approximate value D_m=2.0 has been.

4.5.1 Conversion Between CMD and MMD

One of the convenient properties of the lognormal distribution is that simple formulas relate the median diameters between the various weighted distributions (Hinds, 1982). Examples of weighted distributions include the number distribution as a function of particle size and the mass distribution as a function of particle size, where the same measure of particle size is used in each weighting. For example, to convert from count median diameter (CMD) to a median diameter (QMD) for the distribution weighted by d^Q use:

$$Q\text{MD} = \text{CMD} \cdot exp\left(Q ln^2 \sigma_g\right) \tag{9}$$

where Q is the weighting factor. For solid spherical particles the conversion from CMD to MMD would use Equation (9) with Q=3. Interestingly, the geometric standard deviation remains constant for all the weightings of a lognormal distribution.

In the present case, the particles generated by combustion are certainly not spherical, so that Q must be less than 3. Under the assumption that the agglomerates are fractal, Equation (8) is used to relate DMPS-measured mobility equivalent diameter to particle mass. In this case, the mass fractal dimension is used for the mass weighting (Q=D_m) in Equation (9) so

that the relationship between the DMPS-measured CMD and the MMD for the equivalent mass distribution becomes:

$$\text{MMD} = \text{CMD} \cdot exp\,(D_m ln^2 \sigma_g). \tag{10}$$

Thus, Equation (9) can be used to convert the CMD diameters to MMD for comparison to the MOUDI parameters. Note that MMD is based on mobility equivalent diameter, however, and will be different than the MMAD (based on the aerodynamic equivalent diameter) measured by the MOUDI. A hypothesis for relating these two different median diameters follows.

4.5.2 Conversion Between Mobility and Aerodynamic Equivalent Diameters

The above section considered how to convert between number and mass median diameters where the same characteristic diameter is maintained. Unfortunately, the mass median diameter determined by a DMPS and an impactor can differ because of the very different characteristic sizes measured by each technique. This section proposes a method for converting between the DMPS-measured mobility diameter and the MOUDI-measured aerodynamic diameter.

The discussion of impactor theory in section 4.2 introduced the Stokes number as the dominant parameter that determines impactor performance. All of the discussion, including Equations (3) through (6), assumed spherical particles. In the following derivation, a form for the Stokes number is defined that does not require the assumption of sphericity. This definition of the Stokes number begins with a force balance on a particle moving at low Reynolds number in an arbitrary flow field (neglecting gravitational and buoyancy forces):

$$m_p \frac{dV_p}{dt} = F_{DRAG} = -\frac{3\pi\mu d_{me}}{C(d_{me})}(V_p - V_f) \tag{11}$$

where m_p is the particle mass, V_p and V_f are the particle and fluid velocity vectors, μ is the fluid viscosity, d_{me} is the particle mobility equivalent diameter, and $C(d_{me})$ is the particle slip correction factor. In general, a description for the drag on a nonspherical particle (F_{DRAG}) is a complicated function of particle shape, size, porosity, and orientation. To simplify the analysis, the drag acting on the particle has been equated with the drag on a sphere of the appropriate mobility equivalent diameter, d_{me}, which is the diameter measured by the DMPS (neglecting any preferential orientation during selection, which seems plausible considering the 3-D fractal nature of the agglomerates). In a sense, the DMPS is being used to measure the coefficient multiplying the velocity difference in the right hand expression of Equation (11).

Typically, Equation (11) is nondimensionalized by a characteristic velocity, V_o, and a characteristic time, W/V_o (where W is a characteristic length). As in Equation (3), for impactors the length is taken as the nozzle diameter and the velocity as the average through the nozzle. The resulting nondimensional equation, after simplification, becomes:

$$\frac{d\hat{V}_p}{d\hat{t}} = -\frac{3\pi\mu d_{me} W}{C(d_{me})\, m_p V_o}(\hat{V}_p - \hat{V}_f) = -\frac{1}{St}(\hat{V}_p - \hat{V}_f) \tag{12}$$

where a generalized Stokes number has been introduced:

$$St = \frac{C(d_{me})\, m_p V_o}{3\pi\mu d_{me} W} \tag{13}$$

and where the hat is used to denote dimensionless quantities. Equations (12) and (13) imply that two particles with the same value of *St* will behave identically in the same flow field (i.e. in the MOUDI impactor). Note that Equation (13) is simply a generalization for nonspherical particles of the *St* given earlier: Equation (3) for a spherical particle is recovered if $\frac{\pi}{6}\rho_p d_p^3$ is used for the particle mass in Equation (13). For a fractal agglomerate characterized by the expression $m_p = \beta d_{me}^{D_m}$ the Stokes number becomes:

$$St = \frac{C(d_{me})\, \beta\, d_{me}^{D_m - 1} V_o}{3\pi\mu W} \tag{14}$$

Now, two particles of different shape, size, or density, will behave the same in an impactor if they have the same value of *St*. Therefore, to obtain an expression relating aerodynamic and mobility equivalent diameters, we equate the *St* for a spherical particle of unit density (ρ_o=1 g/cm^3) (the definition of aerodynamic diameter) given by Equation (3) with the *St* for a fractal particle given by Equation (14) to obtain:

$$d_{ae} = \sqrt{\frac{6\beta\, C(d_{me})}{\pi\rho_o\, C(d_{ae})}} \cdot d_{me}^{\frac{1}{2}(D_m - 1)} \quad . \tag{15}$$

If both the mobility and aerodynamic equivalent diameters are measured for the same aerosol, then the coefficient β can be found from:

$$\beta = \frac{\pi}{6} \frac{d_{ae}^2}{d_{me}^{D_m - 1}} \frac{C(d_{ae})}{C(d_{me})} \quad . \tag{16}$$

Note that both Equations (15) and (16) require a calculation the ratio of slip factor based on aerodynamic diameter to the slip factor based on mobility diameter. In the present work, the measured median particle diameters are of order one micron, for which the slip coefficient is close to unity and weakly dependent on diameter. Thus, the slip ratio in Equations (15) and (16) are taken as unity in all of the calculations which follow.

Under the assumption that the mass fractal D_m equals two, it is seen from Equation (15) that the aerodynamic diameter varies as approximately the square root of the mobility equivalent diameter. It can be shown that the conversion from a lognormal mass distribution based on mobility equivalent diameter to a mass distribution based on

aerodynamic equivalent diameter results in a lognormal distribution where the MMAD is obtained from the MMD according to Equation (15) and where the standard deviation is obtained from:

$$\sigma_{ae} = \sigma_g^{\frac{(D_m - 1)}{2}} \quad . \tag{17}$$

For a fractal dimension of two, the expected standard deviation of the mass distribution should be much smaller when expressed in terms of aerodynamic diameter than in terms of the mobility diameter. In practical terms, the mass distribution for the same aerosol should appear much narrower when plotted in terms of aerodynamic diameter than when plotted in terms of the mobility equivalent diameter.

Based on the above discussion, it is easily shown that the relationship between a particle's mass and its aerodynamic diameter is also fractal, although the fractal dimension does not equal two. To see this, solve Equation (15) for d_{me} in terms of d_{ae} and substitute into Equation (8) to show that:

$$m_p = \beta' \cdot d_{ae}^{\frac{2D_m}{D_m - 1}} \quad . \tag{18}$$

Based on Equation (9), the conversion from count median to mass median aerodynamic diameter can be written as:

$$MMAD = CMAD \cdot exp\left(\frac{2D_m}{D_m - 1} ln^2 \sigma_g \right) \quad . \tag{19}$$

In summary, it is valuable to review the assumptions leading to the above results: 1) Equation (9) is a purely mathematical result requiring only that the distribution be lognormal, 2) Equation (9) assumes a lognormal distribution of agglomerates for which the mobility equivalent (DMPS-measured) size and the particle mass are related by a mass fractal D_m, and 3) Equation (9) assumes all of the above plus the relationship between DMPS and aerodynamic diameters hypothesized above.

4.5.3 Comparison of Lognormal Parameters

The above discussion has been used to compare the aerosol distributions obtained using the MOUDI and the DMPS. In Table 4, the MOUDI parameters are presented without manipulation. For the DMPS data, the CMD has been converted to MMD using Equation (9) with an assumed fractal dimension of 2.0. With an assumed fractal dimension, the remaining unknown β is then found for each run using Equation (16) where the slip ratio has been set to unity. Ideally, β should be constant; the values for β in Table 4 agree within experimental uncertainty. Thus, the data are at least consistent with the fractal model proposed above. Interestingly, the DMPS predictions for MMD are as much as a factor of three greater than the MMAD predicted by the MOUDI. Thus, the same particle would be

given a significantly larger size in the DMPS than in an impactor. This result is consistent with the observation that the DMPS preimpactor - with a nominal aerodynamic cutpoint of 0.89 μm - was found to remove relatively few particles even when the DMPS best-fit size distribution showed the majority of particles larger than the impactor cutpoint.

Interestingly, the most consistent agreement for β among the three tests was found with assumed fractal dimensions much larger than 2.0; direct observations of the particles indicate that this is probably too high a value. Typically, SEM images of particles with a fractal dimension less than about two appear two-dimensional, *i.e.*, there is no observable overlap and all of the particle is easily seen. For fractal numbers larger than two, parts of the particle will be obscured by other parts. SEM photographs of collected particles from these tests (such as Figure 1) display a very open structure, so that almost all of the structure is very easily observed.

Table 4: Comparison of MOUDI and DMPS lognormal parameters.

	MOUDI		DMPS[a]				
Run ID URAN	MMAD (μm)	σ_{ae} (-)	CMD (μm)	σ_g (-)	MMD (μm)	β (g/cm^{Dm})	σ_{ae} (-)
135	0.47	2.20	-	-			
136	0.48	2.39	0.56	1.86	1.21	1.21×10^{-5}	1.36
145	0.64	2.06	0.82	1.79	1.62	1.54×10^{-5}	1.34
150	0.63	1.99	0.93	1.80	1.86	1.33×10^{-5}	1.34

a. D_{max}=4.0 μm, D_m=2.0

The standard deviation found for the DMPS distribution can be converted to a standard deviation based on aerodynamic diameter with Equation (17). The disagreement between the MOUDI and DMPS-predicted values for σ_{ae} is significant and not understood. The use of the ideal cut-point method in reducing MOUDI data will tend to widen the distribution compared to the true distribution, but we do not believe that this effect is sufficient to explain the observed differences. This marked difference could indicate a problem with the simple models proposed above.

4.6 MASS LOSS RATE

Although the data is limited, the mass loss rate can be estimated from the MOUDI samples. As seen in Table 2, the two early-time MOUDI samples (URAN.135 and URAN.136, taken 5 minutes after launch) are in good agreement with a total collected mass of about 2.2 mg. The two late-time MOUDI samples (URAN.145 and URAN.150 where the CNC/DMPS samples started 54 minutes after launch, with the MOUDI sample taken 72 minutes after launch) are also in good agreement with a collected mass of about 1.4 mg. The reduction in collected mass results from a significant reduction in mass suspended in the chamber during the 18 minutes of CNC/DMPS sampling. Part of the mass is removed directly by

sampling, and part is removed by deposition to the walls. Thus, a correction is needed to account for the mass removed by CNC/DMPS sampling, which removed about 4.8 liters. Assuming a well-stirred chamber with a total volume of 48.6 liters and a sampling rate of 0.268 liters/minute (which gives an exponential sampling loss coefficient of about 0.0055 min^{-1}), approximately 10% of the total suspended mass would have been removed during the 18 minutes of CNC/DMPS sampling. Assuming a constant exponential loss coefficient over the first 54 minutes (no sampling), and that this loss coefficient can be added to the 0.0055 min^{-1} sampling coefficient for the next 18 minutes (CNC/DMPS sampling), a loss coefficient due to wall loss mechanisms is found to be 0.0049 min^{-1}. This result is approximate, since the wall losses will depend on the nature of the size distribution which is evolving in time. For settling (which is a likely candidate accounting for mass losses), the loss rate should increase as the size distribution grows due to coagulation.

For comparison, a simple analytic model describing settling losses for lognormal distributions is developed here. In general, the mass loss rate of particles in a well stirred chamber is:

$$\mathcal{V}\frac{dC_M}{dt} = -A\,C_M\int_0^\infty V_S\,f_M(d_{ae})\,dlnd_{ae} \tag{20}$$

where $\mathcal{V}$ is the chamber volume, C_M is the particle mass concentration (e.g. mg/cm^3), A is the chamber floor area, V_S is the particle settling velocity, and f_M is the aerodynamic mass distribution given in Equation (7). The settling velocity is a function of aerodynamic diameter given by:

$$V_S = \frac{\rho_o d_{ae}^2 C(d_{ae})\,g}{18\mu} \tag{21}$$

where ρ_o is density of water and g is the gravitational acceleration. For a lognormal distribution, the above two equations can be combined and simplified to yield:

$$\frac{dlnC_M}{dt} = -\frac{1}{H}\frac{\rho_o g}{18\mu}\cdot \mathrm{MMAD}^2\cdot exp\,(2ln^2\sigma_{ae}) \tag{22}$$

where H is the height of the chamber (7-5/8 inches). The right hand side of Equation (22) gives an analytic approximation for the exponential loss coefficient. Using the MOUDI parameters from Table 4 for the early and late time samples gives a loss coefficient of 0.0085 and 0.010 min^{-1}, respectively. These values are clearly too high compared with the observed mass loss coefficients. Using the MMAD from the MOUDI and the σ_{ae} calculated from the DMPS, however, gives early and late-time loss coefficients of 0.0046 and 0.0044 min^{-1}. These values are essentially equal and are in reasonable agreement with the observed mass loss rate of 0.0049 min^{-1}. As stated above, the differences between the MOUDI and DMPS measurements of σ_{ae} cannot be explained, and so it is difficult to say if the simple model given by Equation (22) is adequate. Finally, one supporting argument for a constant loss rate is the observation that the large-particle tails for the early and late-time MOUDI mass distributions are essentially indistinguishable.

4.7 IMPLICATIONS FOR DMPS PREIMPACTOR PERFORMANCE

The DMPS used in these tests was preceded by a single-stage impactor with a nominal aerodynamic cut-point diameter of about 0.89 μm (to remove multiply charged particles and to provide the proper pressure drop to operate the DMPS at low flow rates). However, the reported cut-point diameter assumes a spherical particle for which a simple relationship between the DMPS (mobility) and MOUDI (aerodynamic) diameters exists. For the fractal agglomerates of this study, however, no simple relationship exists between these diameters. However, the model outlined in Section 4.5.2 can be used to arrive at such a relationship under several assumptions and is given in Equation (15). Using this relationship, an assumed mass fractal dimension of 2.0, and the value for β from Table 4, the preimpactor cutpoint in terms of the mobility equivalent diameter becomes about 4 μm. The implications of the preimpactor to DMPS data analysis is considered in Appendix B.

4.8 DISCUSSION OF MOUDI RESULTS

The successful application of the MOUDI in measuring this combustion generated aerosol has significantly added to our understanding in several ways. First, the MOUDI tests provide the first description of this aerosol in terms of a mass distribution based on aerodynamic diameter. The distribution of mass is essential in interpreting ensemble techniques (such as filter samples) which typically measure total mass. A description based on aerodynamic diameter is valuable as it is the appropriate characteristic diameter which governs inertial processes, such as sampling and transport efficiency, human respiration, and gravitational sedimentation. A mass distribution based on aerodynamic diameter is also needed in describing sedimentation losses within the sample chamber. The distributions provided by the MOUDI complement the data from the DMPS and CNC, which provide a number distribution based on mobility diameter which is needed to explore coagulation and diffusion.

Direct comparisons between the DMPS and MOUDI require various assumptions regarding the fractal nature of the agglomerates and their size distribution. Under the lognormal assumption (which seems to hold acceptably well for the present aerosol), well-established formula relate the count and mass median diameters for the same equivalent diameter (e.g., for converting between account and mass median aerodynamic diameters). The comparison between mobility (DMPS-measured) and aerodynamic (impactor-measured) diameters requires additional analysis. Here, a new analysis is presented that is based on the assumption that the aerosol is fractal. The resulting analysis provided expressions (Equations (15) and (16)) that relate aerodynamic and mobility diameters and geometric standard deviations. Using this analysis and an assumed mass fractal dimension of two, the proportionality constant relating particle size and mass (see Equation 8) can be estimated. Calculations of the proportionality constant are in good agreement for different MOUDI size distributions (corresponding to samples taken soon after and long after launch). This agreement provides some support for the various assumptions. One striking result of this work is that the same particle will be sized about three times larger in the DMPS than in the MOUDI. The widths of the corrected-DMPS and MOUDI distributions are not in agreement; the cause of this discrepancy is not yet understood.

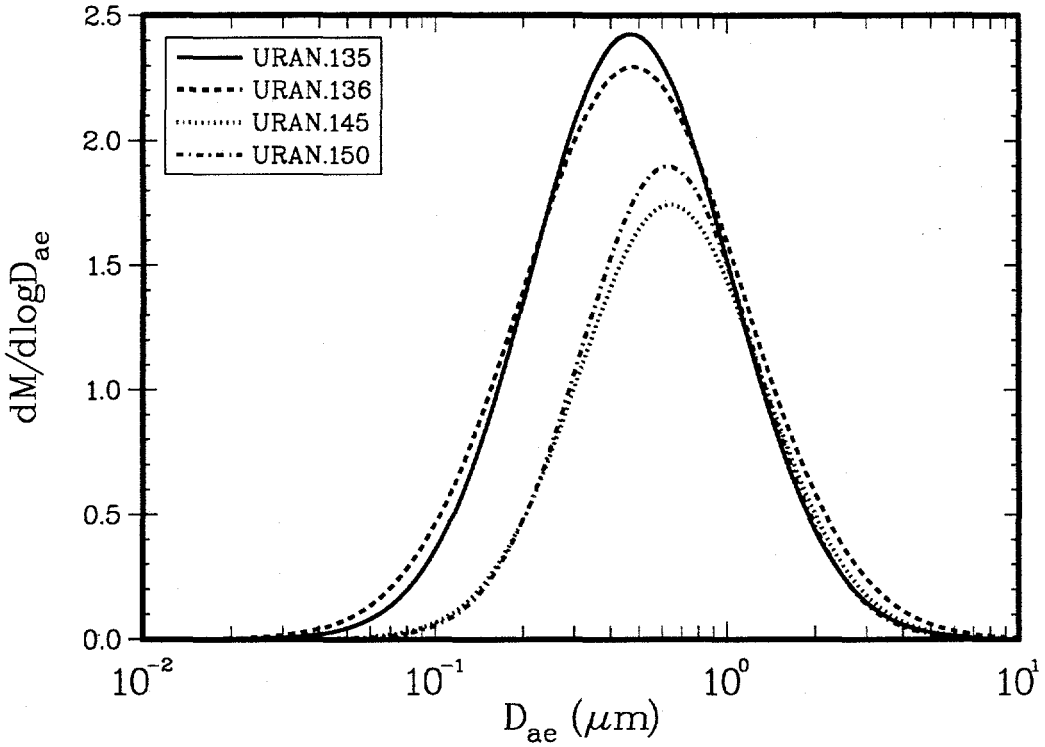

Figure 11. Comparison of lognormal fits for the two early-time (URAN.135 and .136) and late-time (URAN.145 and .150) MOUDI tests.

The implication of the above observations to field work is that, for fractal particles generated by combustion, care must be taken in data interpretation and model development. For example, the same fractal particle requires a different equivalent diameter to predict its coagulation rate than to predict its sedimentation rate. In the present work, factors of up to three differences have been observed between these diameters. Similarly, different measurement techniques will measure different equivalent diameters. Models presented above may be of value for interpreting such measurements.

Finally, comparison of early and late time distributions confirms observations based on DMPS measurements: that the aerosol median diameter increases and the geometric standard deviation decreases with time. Figure 11 compares the two early and the two late time tests. The shift to larger sizes is quite evident, although the narrowing of the distribution is not. In Figure 11 it appears that the large particle tails of all four distributions are essentially identical, indicating that removal by sedimentation may dominate other processes for the larger particles.

5.0 CONCLUSIONS

This report reviewed an experimental study of the aerosol production from the high-velocity combustion of uranium-1.5 wt% molybdenum alloy droplets. An electromagnetic launcher was used to simultaneously heat to melting and electromagnetically propel uranium alloy wires at velocities of about 100 m/s. After launch, the combustion products that are left behind in the droplet wakes cool and condense on existing particles or nucleate to form very high concentrations of ultrafine particles. These primary particles rapidly coagulate to form the web-like agglomerates. Simultaneously, mixing acts to spread the particles around the chamber. Even after the aerosol is mixed throughout the entire chamber volume, concentrations are high enough that coagulation continues to occur. The size distribution also changes due to loss mechanisms, including particle removal by the sampling equipment and particle losses to the chamber walls by sedimentation and diffusion. This work applied a variety of aerosol diagnostics to provide as much information as possible regarding the aerosol dynamics taking place within the chamber.

Direct concentration measurements with a CNC provided several valuable insights into the dynamics of this combustion-generated aerosol. Most important is that the concentration is not constant, but decays with time as a result of coagulation, sampling losses, and wall losses. The most rapid decay is seen immediately after launch, when the combination of small particle size and high concentration leads to rapid coagulation. An approximate model that includes coagulation, wall losses, and sampling losses was proposed to describe the dynamics of the concentration decay. Soon after launch coagulation dominates, and a best-fit coagulation coefficient for this time is about 1×10^{-7} cm^3/min. Although there is a large uncertainty in this value, it is significantly greater than for spheres with the same DMPS-measured diameters. Thus, coagulation rates of similar aerosol in the field may be significantly higher than expected. The cause of this enhancement is likely the chain agglomerate structure of the particles, which creates more surface area per unit particle volume. The model also does a good job of describing late-time losses, which are dominated by the sampling of aerosol from the chamber to make measurements. Thus, at late times both wall losses and coagulation can be neglected. One concern is the relatively large fluctuations observed during the CNC tests, which suggests that the sampling chamber was not well mixed under some conditions.

DMPS tests supported several earlier observations and also provided new results. As shown for other metals, the agglomerates generated by the high-velocity combustion of uranium alloy droplets can be adequately described by a simple lognormal distribution. The size distributions are very similar to those observed for earlier tests with tungsten: both give early-time CMDs of 0.3 - 0.4 μm with geometric standard deviations of about 2, although concentrations for the tungsten tests were at least two orders of magnitude less than in the present uranium tests. A major advance in the present work was the use of a new charging algorithm, which greatly improved the agreement between DMPS best-fit predictions and CNC direct measurements of the total concentration. In addition, DMPS measurements have demonstrated that the size distribution grows in size and narrows in spread when coagulation is active.

The successful application of the MOUDI in measuring this combustion generated aerosol has significantly added to our understanding in several ways. First, the MOUDI tests provided the first description of this aerosol in terms of a mass distribution based on aerodynamic diameter. Comparison of early and late time distributions confirms several observations based on DMPS measurements: lognormal size distributions that show increasing aerosol median diameter and decreasing geometric standard deviation with time due to coagulation. The rate of growth in terms of aerodynamic diameter, however, is much less than that in terms of mobility diameter. It also appears that the large-particle tails of both early- and late-time distributions are essentially identical, suggesting that removal by sedimentation dominates other processes for the larger particles.

Direct comparisons between the DMPS and MOUDI require various assumptions regarding the fractal nature of the agglomerates and their size distribution. Under the lognormal assumption (which seems to hold acceptably well for the present aerosol), well-established formula relate the count and mass median diameters for the same equivalent diameter (e.g., for converting between aerodynamic count and mass median diameters). The comparison between mobility (DMPS-measured) and aerodynamic (impactor-measured) diameters requires additional analysis. Here, a new analysis is presented that is based on the assumption that the aerosol is fractal. The resulting analysis provided expressions that relate aerodynamic and mobility diameters and geometric standard deviations. Using this analysis, estimates are made of the proportionality constant relating particle mobility and mass. One striking result is that the same particle will be sized about three times larger in the DMPS than in the MOUDI. The widths of the corrected-DMPS and MOUDI distributions are not in agreement; the cause of this discrepancy could either be experimental or model-related.

A major outcome of this work is that, due to the nonspherical nature of this aerosol, different "diameters" are required to describe each of the various mechanisms controlling the size distribution. Thus, the same agglomerate may settle under gravity at the same speed as a 1 μm sphere, while it diffuses at the same rate as a spherical particle several times larger. Although these issues were dealt with in the context of describing the aerosol evolution within the chamber, it should be emphasized that the same issues will arise in predicting the aerosol behavior in field environments. For example, dispersal characterization under accident scenarios and reconstruction of the initial size distribution from particle samples collected from the debris cloud frequently require simultaneous modeling of coagulation, diffusion, and sedimentation. The present work has attempted to provide methods for converting between the various equivalent diameters required for these calculations.

Several difficulties were encountered during these tests. Of greatest concern are the relatively large concentration fluctuations observed during the tests, which suggests that the sampling chamber was not well mixed. For future tests, methods for enhancing mixing should be explored. A second area of experimental improvement would be to include a dilution system for working at the higher concentrations. In the present setup, direct sampling leads to rapid fouling of the internal CNC filters. Finally, additional work remains to link the particle size observed under SEM analysis to the mobility and aerodynamic diameters measured here.

6.0 REFERENCES

1. Benson, D.A. and Rader, D.J. (1986) "A High Velocity Electromagnetic Particle Launcher for Aerosol Production Studies," Sandia National Laboratories Report SAND86-0365, Albuquerque, NM.

2. Benson, D.A. and Rader, D.J. (1990) "Electromagnetic Launcher Studies of Breakup and Aerosol Formation in Molten Uranium Alloy," Sandia National Laboratories Report SAND90-0021, Albuquerque, NM.

3. Bevington, P.R. (1969) *Data Reduction and Error Analysis for the Physical Sciences,* McGraw-Hill Book Company, New York.

4. Gunn, R. (1955) "The Statistical Electrification of Aerosols by Ionic Diffusion," *J. Colloid Sci.* **10**: 107-119.

5. Hering, S.V. and Marple, V.A. (1986) *Cascade Impactor: Sampling and Data Analysis* (J.P. Lodge and T.L. Chen, eds.) American Industrial Hygiene Association, Akron, Ohio, pp. 103-127.

6. Hinds, W.C. (1982) *Aerosol Technology,* John Wiley & Sons, Inc., New York.

7. Marple, V.A., Rubow, K.L., and Behm, S.M. (1991) "A Microorifice Uniform Deposit Impactor (MOUDI): Description, Calibration, and Use," *Aerosol Sci. Technol.* **14**: 434-446.

8. Rader, D.J. (1990) "Momentum Slip Correction Factor for Small Particles in Nine Common Gases," *J. Aerosol Sci.* **21**: 161-168.

9. Rader, D.J. and Benson, D.A. (1988) "Aerosol Production by High-Velocity Molten-Metal Droplets," Sandia National Laboratories Report SAND88-0678, Albuquerque, NM.

10. Reist, P.C., Hsieh, M.T., and Lawless, P.A. (1989) "Fractal Characterization of the Structure of Aerosol Agglomerated Grown at Reduced Pressure," *Aerosol Sci. Technol.* **11**: 91-99.

11. Rogak, S.N. and Flagan, R.C. (1992) "Bipolar Diffusion Charging of Spheres and Agglomerate Aerosol Particles," *J. Aerosol Sci.* **23**: 693-710.

12. Schaefer, D.W. and Hurd, A.J. (1990) "Growth and Structure of Combustion Aerosols: Fumed Silica," *Aerosol Sci. Technol.* **12**:876-890.

13. Schmidt-Ott, A., Baltensperger, U., Gaggeler, H.W., and Jost, D.T. (1990) "Scaling Behaviour of Physical Parameters Describing Agglomerates," *J. Aerosol Sci.* **21**(6): 711-717.

14. Wiedensohler, A. (1988) "An Approximation of the Bipolar Charge Distribution for Particles in the Submicron Range," *J. Aerosol Sci.* **19**: 387-389

15. Witten, T.A., and Sander, L.M. (1981) "Diffusion-limited Aggregation, a Kinetic Critical Phenomenon," *Phys. Rev. Letters* **47**: 1400-1403.

Appendix A. Summary of Test Series

Table 5: Summary of launcher tests for which aerosol data was taken.

RUN ID	Aperture (inches)	CNC	DMPS	MOUDI	ESP	Comments
URAN.111	0.25		X			TDMA
URAN.112	0.125		X			
URAN.113	0.25		X			Overnight
URAN.114	0.25		X			TDMA
URAN.115	0.25		X			TDMA
URAN.116	0.25		X			Filter
URAN.117	0.25		X			Filter
URAN.118	0.25		X			Charging study
URAN.121	0.25	LOW[a]	X			Overnight
URAN.122	0.25	HIGH[b]	X			
URAN.123	0.25	HIGH	X		X	TEM
URAN.124	0.25	LOW				
URAN.125	0.25	HIGH	X			Overnight
URAN.126	0.25	HIGH	X			
URAN.127	0.25	HIGH				
URAN.128	1.0	HIGH	X			Overnight
URAN.129	1.0	HIGH	X			
URAN.130	0.25		X		X	TEM
URAN.131	0.25		X		X	TEM
URAN.132	0.25		X		X	TEM
URAN.133	1.0			X		No rotation
URAN.134	1.0			X		No rotation
URAN.135	1.0			X		Early-time
URAN.136	1.0		X	X		Early-time
URAN.139	0.25		X			Filter

Table 5: Summary of launcher tests for which aerosol data was taken.

RUN ID	Aperture (inches)	CNC	DMPS	MOUDI	ESP	Comments
URAN.140	0.25		X			Filter
URAN.141	0.25		X		X	TEM
URAN.142	0.25		X		X	Launch in nitrogen
URAN.143	0.25	HIGH	X			Launch in nitrogen
URAN.144	1.0		X	X		Residue from 143
URAN.145	1.0		X	X		Late-time
URAN.146	1.0		X			Overnight
URAN.147	1.0		X	X		MOUDI plugged
URAN.148	1.0		X			Launch in CO_2
URAN.149	1.0		X		X	Launch in CO_2
URAN.150	1.0		X	X		Late-time

a. CNC operated at low flowrate, 0.268 lpm
b. CNC operated at high flowrate, 1.32 lpm

Appendix B. Improvements to DMPS Data Analysis

A detailed discussion of the data inversion method used in the present study is found in Appendix A of Rader and Benson (1988). The purpose of the inversion is this: given a set of observed concentrations exiting the electrostatic classifier (the mobility distribution), find the number distribution that best describes the observations. The inversion process applied here requires several components: 1) an expression relating particle size and electric mobility, 2) a theoretical description of the mobility response function (which describes what mobility particles are selected for a given set of DMPS conditions), 3) a functional form for the unknown size distribution, and 4) a size-dependent expression for the charge distribution which relates the fraction of particles carrying a specific charge. Items 1 and 2 are dealt with exactly as described in Rader and Benson (1988). The assumed size distribution and the charging mechanism are discussed in detail below. In addition, the present experimental set-up used a preimpactor that was not present in the previous work; the implications of this added piece of equipment to data inversion is also discussed below. A brief discussion of some of the experimental checks made on the data acquisition/ inversion process are presented in the main body (Section 3.3).

B.1 Lognormal Distribution

The functional form of the size distribution is assumed to be lognormal. This choice was heavily influenced by the earlier work (Rader and Benson, 1988) which showed that the lognormal provides a very good description of the observed tungsten and zirconium aerosol distributions. As will be seen, the lognormal also seems to describe the size distributions observed in the present study of the aerosol generated by uranium combustion. The form of the lognormal is presented here for reference:

$$dN = \frac{N_T}{\sqrt{2\pi}\,\ln\sigma_g} exp\left[-\frac{(\ln d_{me} - \ln CMD)^2}{2\,(\ln\sigma_g)^2}\right] d\ln d_{me} \quad . \tag{B.1}$$

where dN is the number of particles with (mobility-equivalent) diameters between $\ln d_{me}$ and $\ln d_{me}+d\ln d_{me}$, N_T is the total number concentration of particles suspended in the chamber, CMD is the count median mobility equivalent diameter and σ_g is the geometric standard deviation based on the mobility equivalent diameter.

With the lognormal assumption, the determination of the number distribution reduces to the problem of finding the three parameters, N_T, CMD, and σ_g, that best describe the observed DMPS measurements. To find these parameters a nonlinear least-squares minimization method (Bevington, 1969) is used in which Equation (7) (with assumed initial values for the parameters N_T, CMD, and σ_g), the charging law (see below), and the DMPS response function (see Rader and Benson, 1988) are combined as given in Rader and Benson (1988). The minimization then seeks the values of the three parameters that minimize the sum of squared differences between the predicted and observed concentrations. Two weighting options were used in analyzing the data. The first was to use no weighting (MODE=0),

which in practice forces the fitting to most closely match the high-concentration data. This weighting was typically used for high concentrations where the size distribution changes rapidly. A statistical weighting (MODE=-1) was used at low concentrations to minimize counting errors. Discussion of the weighting functions is available in Bevington (1969).

B.2 Charge Distribution

The Boltzmann-Gunn charge distribution used in the earlier work (Rader and Benson, 1988) has been replaced in this study with a new charge distribution based on the recent work of Wiedensohler (1988). Wiedensohler uses two expressions to cover the size and charge range of interest. First, for particles larger than one micron (all charge states) and for particles less than one micron carrying three or more charges, the following result due to Gunn (1956) for the fraction of particles of diameter d_p and carrying charge γ is used:

$$\Phi_\gamma(d_p) = \frac{1}{\sqrt{2\pi a}} exp\left[\frac{(\gamma - a\sigma)^2}{2a}\right] \tag{B.2}$$

where:

$$a = \frac{d_p kT}{2e^2}$$

is a dimensionless size (k is Boltzmann's constant, T is the temperature, and e is the fundamental charge) and σ is a factor accounting for charge asymmetry taken by Wiedensohler as -0.134. The Gunn equation is basically a modification of the Boltzmann equation (used in the earlier inversion method, and obtained by setting σ to zero in the above equation) that accounts for the charge asymmetry observed in real systems (i.e., there are unequal numbers of particles carrying +1 and -1 elementary charges). For particles smaller than one micron and carrying +1 or +2 charges, Wiedensohler (1988) proposed the following correlation:

$$\Phi_\gamma(d_p) = 10^{\left[\sum_{i=0}^{5} a_i(\gamma)\ (\log d_p)^i\right]} \tag{B.3}$$

where d_p is input in nanometers. Wiedensohler obtained the coefficients a_i by least-square regression analysis to his calculations based on the Fuchs charging theory. Unfortunately, errors were found in the published coefficients during the course of this study; we reevaluated Wiedensohler's data and the best-fit coefficients used in this study are given in Table 1. Agreement between Equation (B.3) with the present coefficients and the tabulated Fuchs-theory calculations of Wiedensohler is very good.

Strictly speaking, the above charging expressions only apply for spherical (or nearly spherical particles); it is not obvious which appropriate equivalent diameter should be used in calculating the charge fraction for the present agglomerates. As in our previous work, the diameter used in the charging correlations is taken as the electric mobility diameter, d_{me}.

The validity of this assumption has also been suggested by other experimentalists (Rogak and Flagan, 1992), but is by no means proven.

For the same data, the change to the Wiedensohler charging mechanism from the previously used mechanism gives number distributions that: 1) have about the same CMD, 2) are slightly narrower, and 3) give a total concentration about 30 to 50% greater than before. As seen in Section (3.3), the higher total concentrations predicted using the new charging mechanism are in good agreement with direct CNC measurements.

Table 6: Coefficients used in charge distribution correlation.

$a_i(\gamma)$	γ=1	γ=2
a_0	-2.3484	-8.97763
a_1	0.6044	-3.41789
a_2	0.4800	13.1083
a_3	-0.00124	-7.89172
a_4	-0.1544	1.89666
a_5	0.0320	-0.166323

B.3 Preimpactor Cut-point Diameter

A second change from earlier work is that the DMPS used in these tests was preceded by a single-stage impactor (preimpactor) with a nominal cutpoint diameter of about 0.89 μm (to reduce the number of multiply-charged, large particles and to provide the proper inlet pressure to operate the DMPS at low flow rates). However, the reported cut-point diameter assumes a spherical particle for which a simple relationship between the DMPS (mobility) and preimpactor (aerodynamic) diameters exists. For the fractal agglomerates of this study, however, no simple relationship exists between these diameters. However, as described in subsection 4.5 above, a hypothetical model can be used to arrive at such a relationship under several assumptions. Using the relationship derived in subsection 4.5, an assumed mass fractal of 2.0, and the value for β from Table 4, the preimpactor cutpoint in terms of the DMPS mobility equivalent diameter is about 4 μm. This cutpoint is strictly a best guess, and further work needs to be done to more precisely define it. The data inversion algorithm was altered to include the effect of the preimpactor by including a maximum diameter over which the integral was performed.

For particle distributions with a CMD below about 0.7 μm the presence of the preimpactor had little effect; for larger particles, the exact value of the preimpactor cutpoint becomes more important in determining the best-fit lognormal. Due to the uncertainties in defining the preimpactor cutpoint, distributions with CMDs near one micron should be considered as approximate. In retrospect, since the impactor fails in its intended purpose (to remove particles larger than about one micron), it could be omitted from the experimental setup with little loss and a great gain in simplifying the data inversion.

Appendix C. Cut-point Correction for MOUDI

One complexity with using the MOUDI is that Marple et al. (1991) report the cut-point diameters for a system operating at an ambient pressure of 740 mm Hg. For the current studies (which were conducted in Albuquerque, NM), the ambient pressure is 630 mm Hg and a correction is required. The need for the correction can be found in Equation (5), which shows that the cut-point diameter is implicitly defined in terms of itself through the slip correction factor C. This factor corrects for the noncontinuum drag effects that result as the particle size approaches the mean free path of air (about 0.065 μm at 760 mm Hg and 296K). Since the mean free path depends on pressure, the slip correction also varies with local pressure. For large particles, C tends to unity and can be neglected. For the submicron MOUDI stages, however, the slip correction factor becomes significant and must be included. The critical step is to determine the appropriate pressure to use for each stage. Hering and Marple (1986) suggest that, because of pressure recovery in the stagnation region above the impaction plate, the pressure upstream of the nozzle should be used in calculating the slip factor for each stage. Marple et al. (1991) report the ratio of the pressure after each stage, P, to the ambient (inlet) pressure P_o: these ratios range from 1.0 for the stages with cut-point diameters above 1 μm to 0.53 at the exit of stage B (see Table 1).

Unfortunately, it is not guaranteed that these ratios are themselves independent of inlet pressure and overall flowrate. We have shown[1], however, that both the pressure ratios and the mean jet velocity for each stage are independent of the inlet pressure under the following two conditions: 1) that the volumetric flow rate is kept equal to that in the original calibration (30 liters/minute) and 2) that the pressure drop through an orifice can be accurately approximated by $\Delta P = K\rho V^2$ where K is a constant, and ρ and V are the upstream gas density and mean velocity through the orifice. The first condition is easily met during operation, and the second approximation is consistent with the experimental measurements for pressure drop given by Marple et al. (1991) with K approximately equal to 0.8 for all but the final stage (note that the pressure downstream of the final stage is never used). Thus, the cut-point diameters given in Marple et al. (1991) are corrected for each stage using:

$$d_{ae} = d_{ae50}\sqrt{\frac{C_{50}(d_{ae50}, P_{50})}{C(d_{ae}, P)}} \qquad \text{(C.1)}$$

where the d_{ae50} and P_{50} are Marple's cut-point diameter and upstream (of nozzle) pressure, and d_{ae} and P are the values corrected for Albuquerque operating conditions. Note that the pressure upstream of each nozzle is calculated using the pressure ratios of Table 1 and the local appropriate inlet pressure (P_o=740 mm Hg for Marple and 630 mm Hg for Albuquerque). As is evident, the above equation must be solved iteratively. The expression for the slip correction is that given for air by Rader (1990). The cut-point diameters corrected to Albuquerque ambient pressure are given in Table 1.

1. The complete derivation is lengthy and is not included here.

DISTRIBUTION

Defense Nuclear Agency
6801 Telegraph Road
Alexandria, VA 22310-3398
Attn: TDTR, Maj Jack Deplitch

University of California (6 copies)
Lawrence Livermore National Laboratory
PO Box 808
Livermore, CA 94550
Attn: WED, T. Lindman, L125
Z-Div, B. Weinstein, L377
Z-Div, D. Wright, L387
G-Div, R. Cederwall, L262
G-Div, Ted Harvey, L262
D-Div, Frank Serduke, L84

Los Alamos National Laboratory (7 copies)
PO Box 1663
Los Alamos, NM 87545
Attn: NIS-8, M. MacInnes, MS B228
NIS-9, V.R. Koym, MS B229
NIS-9, G. Strickfaden, MS B229
CST-10, D.Finnegan, MS J514
DX-11, A.B. Anderson, MS P942
DX-11, D. McClure, MS P940
DX-13, H.H. Watanabe, MS P940

U.S. Department of Energy (5 copies)
Forrestal Building
1000 Independence Ave.
Washington, DC 20585
Attn: NN-20, M. Koontz
NN-20, L. Casey
NN-30, N. Trulock
NN-31, L. Martin
EM-50, C. Frank, 6B-158

U.S. Department of Energy
Albuquerque Operations Office
PO Box 5400
Albuquerque, NM 87115
Attn: WQD, R.J. Lopez

Martin Marietta Corp.
PO Box 8555
Philadelphia, PA 19101
Attn: B. Faust, Bldg 100, Rm M-9425

Pacific Northwest Laboratories (2 copies)
P.O. Box 999
Richland, WA 99352
Attn: J. Wacker, P7-07
B. Wright, P7-07

Westinghouse Hanford Company
P.O. Box 1970
Richland, WA 99352
Attn: B.J. Layman/MSIN L6-12

Lovelace Inhalation Toxicology Research Institute (3 copies)
Albuquerque, NM 87115
Attn: M.D. Hoover
G.J. Newton
H.C. Yeh

MS 0492	12324	P.A. D'Antonio
MS 0601	1128	P.J. Hargis, Jr.
MS 1082	1333	D.A. Benson (10 copies)
MS 0819	1431	J.M. McGlaun
MS 0819	1431	T.G. Trucano
MS 0819	1431	D.E. Grady
MS 0820	1432	P. Yarrington
MS 0820	1432	M. Kipp
MS 0834	1512	A.C. Ratzel
MS 0834	1512	J.E. Brockmann
MS 0834	1512	D.J. Rader (10 copies)
MS 0437	1518	J.W. Swegle
MS 0337	1800	A.D. Roming, Jr.
MS 0368	1815	J.H. Aubert
MS 0368	1815	H.C. Peebles
MS 0340	1831	M.J. Cieslak
MS 0340	1831	C.V. Robino
MS 0327	2514	A.M. Renlund
MS 0457	5600	D.B. Hayes
MS 0463	5000	R.L. Hagengruber
MS 0469	5006	J.M. Taylor
MS 0570	5900	C.W. Childers
MS 0570	5902	B.F. Johnson
MS 0570	5908	T.P. Wright
MS 0574	5941	L.A. Boye
MS 0840	5931	C.A. Searls
MS 0574	5941	C.S. Lee
MS 0576	5911	J.M. Holovka
MS 0576	5911	W. Caldwell
MS 0576	5911	C.M. Craft (25 copies)
MS 0728	6602	M.M. Hightower
MS 0715	6603	R.E. Luna
MS 0755	6612	A.E. Verardo, Attn: M.W. Moulton
MS 0755	6612	W. Einfeld

MS 0755	6612	B.D. Zak
MS 0899	13414	Technical Library (5 copies)
MS 0619	12613	Technical Publications
MS 9056	8102	M. Lapp
MS 9056	8102	L.R. Thorne
MS 9056	8102	J. Vitko, Jr.
MS 9103	8111	G.A. Thomas
MS 9052	8361	L.L. Baxter
MS 9018	8523-2	Central Technical Files
MS 0567	9241	P.R. Dobranich
MS 0763	9614	B.A. Boughton
MS 0763	9614	M.J. Sagartz
MS 0763	9614	E.J. Graber
MS 0100	7613-2	Document Processing for DOE/OSTI (2 copies)